Advanced nanofibers integrating vitamin D3 and cerium oxide nanoparticles for enhanced diabetic wound healing: Coelectrospun silk fibroin-collagen and chitosan-PVA systems

Zoleikha Azari, Alireza Sadeghi-Avalshahr, Fatemeh Alipour, Bahman Jalali Kondori, Vahid Reza Askari, Sahar Mollazadeh, Simin Nazarnezhad, Seyedeh Najibeh Nasiri, Farzad Kermani, Marziyeh Ranjbar-Mohammadi



PII: S0141-8130(25)03651-7

DOI: https://doi.org/10.1016/j.ijbiomac.2025.143099

Reference: BIOMAC 143099

To appear in: International Journal of Biological Macromolecules

Received date: 25 December 2024

Revised date: 3 April 2025

Accepted date: 10 April 2025

Please cite this article as: Z. Azari, A. Sadeghi-Avalshahr, F. Alipour, et al., Advanced nanofibers integrating vitamin D3 and cerium oxide nanoparticles for enhanced diabetic wound healing: Co-electrospun silk fibroin-collagen and chitosan-PVA systems, *International Journal of Biological Macromolecules* (2024), https://doi.org/10.1016/j.ijbiomac.2025.143099

This is a PDF file of an article that has undergone enhancements after acceptance, such as the addition of a cover page and metadata, and formatting for readability, but it is not yet the definitive version of record. This version will undergo additional copyediting, typesetting and review before it is published in its final form, but we are providing this version to give early visibility of the article. Please note that, during the production process, errors may be discovered which could affect the content, and all legal disclaimers that apply to the journal pertain.

Advanced Nanofibers Integrating Vitamin D3 and Cerium Oxide Nanoparticles for Enhanced Diabetic Wound Healing: Co-Electrospun Silk Fibroin-Collagen and Chitosan-PVA Systems

Zoleikha Azari^{a,b}, Alireza Sadeghi-Avalshahr^{c,d}, Fatemeh Alipour^b, Bahman Jalali Kondori^b, Vahid Reza Askari^e, Sahar Mollazadeh^f, Simin Nazarnezhad^d, Seyedeh Najibeh Nasiri^d, Farzad Kermani^d, Marziyeh Ranjbar-Mohammadi^g*

^a Bhbahan Faculty of Medical Sciences, Behbahan, Iran

g Department of Textile Engineering, University of Bonab, Bonab, Iran Corresponding author: Marziyeh Ranjbar-Mohammadi Corresponding Email address: m.ranbar@ubonab.ac.ir

Abstract

This study investigates the co-electrospinning of polyvinyl alcohol-chitosan (PVA-CS) with cerium oxide nanoparticles (CeNPs) and silk fibroin-collagen (SF-Col) with vitamin D3 for diabetic wound healing applications. The SEM results showed smooth, bead-free nanofiber structures. The diameters of the SF-Col and PVA-CS nanofibers ranged from 168 \pm 51 nm to 1956 ± 450 nm and 211.4 ± 37.2 nm, respectively. By surface modification using fetal bovine serum (FBS), CeNPs dispersion was enhanced. The average diameter of the uniformly distributed fibers on the SF-Co-D/PVA-CS-CeNPs nanofibers was 621.4 ± 50.6 nm. The addition of CeNPs and vitamin D3 improved cytocompatibility at lower doses. The FTIR test confirmed polymer interactions. Contact angle measurements indicated increased hydrophilicity. SEM analysis demonstrated excellent adhesion and growth of L929 fibroblast cells and significant HUVEC migration on SF-Col-D/PVA-CS-CeNP mats, emphasizing their potential to support cell proliferation and tissue regeneration. Blood compatibility assays exhibited hemolysis percentages below 2%, classifying the nanofibers as non-hemolytic. Antibacterial tests revealed significant reductions in Staphylococcus aureus and Pseudomonas aeruginosa survival, addressing infection concerns in chronic wounds. Furthermore, in vivo studies have demonstrated that the utilization of SF-Co-D/PVA-CS-CeNPs nanofibrous membrane as a dressing for full-thickness skin wounds in rats has resulted in accelerated tissue regeneration.

Keywords: Fibroin; Collagen; Chitosan; Vitamin D3; Cerium oxide; Wound Healing

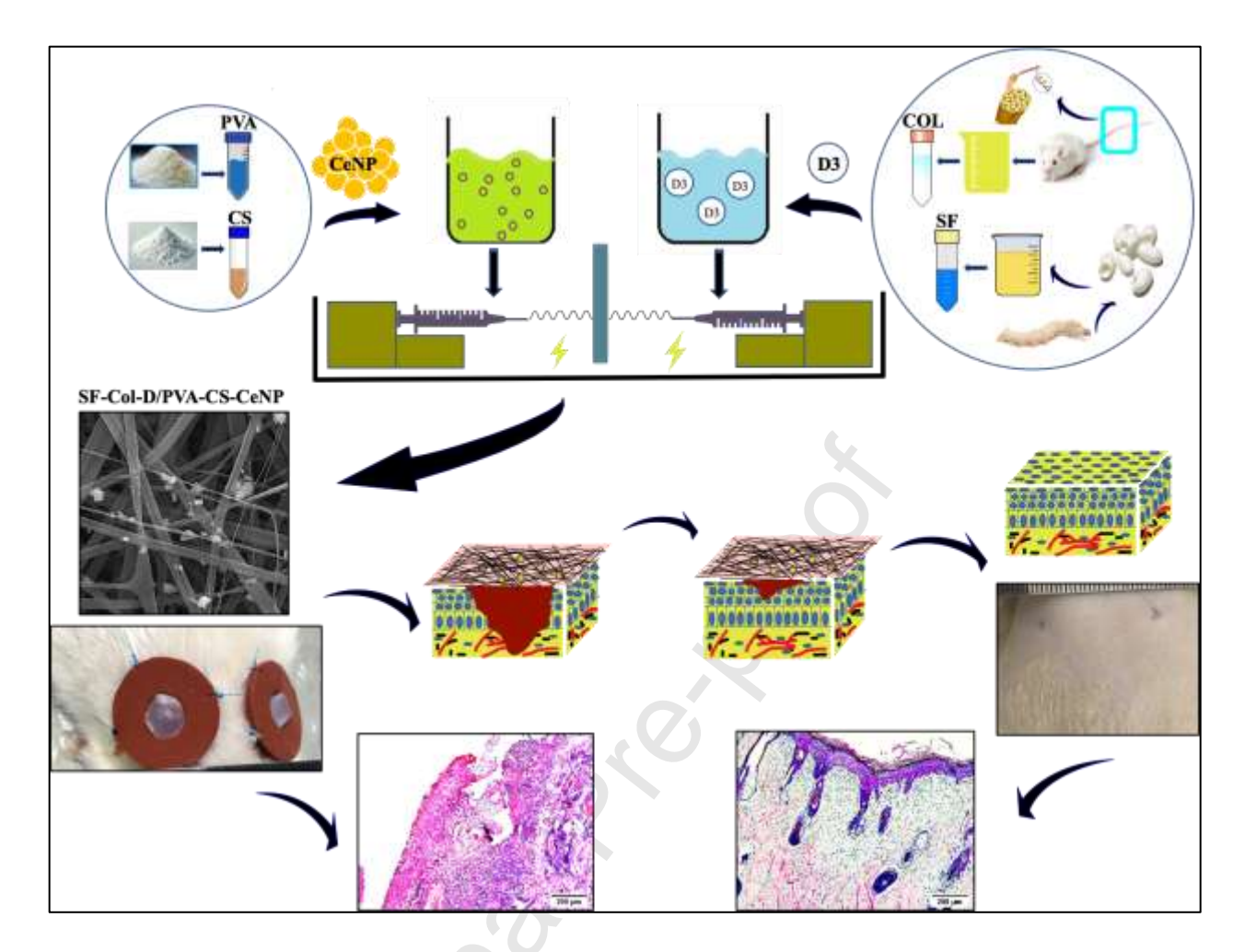
^b Department of Anatomy and Cell Biology, School of Medicine, Mashhad University of Medical Sciences, Mashhad, Iran

^c Department of Materials Research, Iranian Academic Center for Education, Culture and Research (ACECR), Khorasan Razavi Branch, Mashhad, Iran

^d Tissue Engineering Research Group (1), Department of Anatomy and Cell Biology, School of Medicine, Mashhad University of Medical Sciences, Mashhad, Iran

^e Pharmacological Research Center of Medicinal Plants, Mashhad University of Medical Sciences, Mashhad, Iran ^f Department of Materials Engineering, Faculty of Engineering, Ferdowsi University of Mashhad (2), Azadi Sq.,

Mashhad, Iran



1-Introduction

By the year 2045, it is anticipated that approximately 700 million individuals worldwide will be affected by diabetes mellitus (DM), a condition whose prevalence is rising at an alarming rate (3). Nearly 20% of the diabetic population worldwide experiences diabetic foot ulcers (DFU), a prevalent and hazardous consequence of inadequately managed diabetes. The rates of amputation and mortality among patients with DFU are particularly concerning, with incidence figures reported at 19.03% and 16.26%, respectively (4). Given the significant levels of prevalence, morbidity, and mortality, there exists a critical clinical imperative for the effective management and treatment of DFU (4). In light of the limitations previously mentioned, electrospinning has emerged as a prominent technique for the fabrication of porous scaffolds, noted for its

accessibility, cost-effectiveness, and efficiency (5). This technique facilitates the formation of nanofibrous structures that closely mimic the natural extracellular matrix (ECM), thereby providing an optimal environment for cell adhesion, proliferation, and differentiation (5). The initial phase in the electrospinning process involves selecting an appropriate biomaterial for scaffold fabrication, which must be tailored to meet the structural and functional requirements of the target tissue (6). A diverse array of both natural and synthetic polymers has been employed in wound healing, each presenting distinct advantages and limitations. Poly(vinyl alcohol) (PVA) is a synthetic polymer approved by the FDA (Food and Drug Administration) and is esteemed for its high tensile strength, flexibility, non-toxicity, biodegradability, cytocompatibility, and solubility in water, rendering it particularly suitable for applications in skin tissue engineering (7, 8). Chitosan (CS), extracted from the shells of marine crustaceans, is acknowledged for its appropriateness in skin tissue engineering due to its exceptional biocompatibility, biodegradability, and potent antibacterial properties (9).

Silk fibroin (SF) is a naturally occurring protein extracted from various sources, including scorpions, spiders, bees, and the cocoons of silkworms, particularly *Bombyx mori*. (10, 11). The remarkable biocompatibility, biodegradability, and optimal water vapor permeability of SF position it as a promising biomaterial for electrospinning in applications related to wound healing (10, 12). Collagen I (Col I), which constitutes approximately 30% of the total protein composition in the human body, is recognized as the most abundant protein, playing a crucial role in providing biomechanical properties and functional integrity to diverse tissues, including bone, ligaments, and skin (13, 14). Rat tail tendons are commonly utilized as a source of Col type I in laboratory environments. Their elevated concentration of collagen, coupled with the ease of isolation and availability—often as surgical remnants from animal experiments—renders

tendons the preferred tissue for collagen extraction (14). The incorporation of additives such as pharmaceuticals, nanoparticles, and cells into electrospun material blends can substantially augment the clinical applications of scaffolds. This integration promotes the development of multifunctional scaffolds that not only support tissue engineering but also facilitate targeted drug delivery, enhance cellular interactions, and foster overall tissue regeneration (15). The sustained release of pharmaceuticals is critical for their effective clinical application. Recent scholarly interest has increasingly focused on polymer-based drug delivery systems (DDS) that utilize nanofibers (16-19). Due to their distinctive size and morphology, nanofibers demonstrate a superior drug encapsulation capacity compared to other nanomaterials, thereby enhancing their efficacy as drug delivery systems. Vitamin D3 plays an essential role in various skin functions, including the proliferation and differentiation of keratinocytes, as well as the regulation of immune responses(20). Furthermore, research has indicated that cerium oxide nanoparticles (CeNPs) are promising agents for the prevention of bacterial infections and the enhancement of angiogenesis in skin wounds (21).

The significance of this study resides in its innovative exploration of SF-Col and PVA-CS hybrid nanofibers, fabricated through a dual electrospinning technique to improve their morphology and cytocompatibility for tissue engineering and wound healing applications. In distinction to existing literature, this research methodically investigates the implications of varying polymer concentrations, the incorporation of vitamin D3, and the addition of CeNPs on fiber characteristics and biological performance. The stable and controlled release profiles of vitamin D3 and CeNPs further affirm the promise of these materials for biomedical applications, positioning this work as a substantial contribution to the advancement of biomaterials with enhanced therapeutic properties. The co-electrospinning technique allows for meticulous control

over fiber morphology, composition, and agent distribution, providing an advanced method for integrating multiple bioactive agents, such as vitamin D3 and CeNPs. Compared to conventional techniques, co-electrospinning ensures a more homogeneous distribution of agents, improved release profiles, and enhanced biocompatibility, rendering it ideally suited for advanced wound healing applications. The findings underscore the potential of this methodology for developing multifunctional biomaterials aimed at tissue regeneration. It is hypothesized that the co-electrospinning of SF-Col nanofibers with vitamin D3 and PVA-CS nanofibers containing CeNPs will yield a scaffold that exemplifies enhanced cytocompatibility, antimicrobial activity, and wound healing efficacy. These improvements are anticipated to arise from the synergistic effects of refined fiber morphology, increased hydrophilicity, controlled therapeutic release, and the bioactivity of the incorporated agents, facilitating cell adhesion, proliferation, and tissue regeneration. The outcomes of this study are expected to contribute to the development of an advanced wound dressing based on SF-Col-D/PVA-CS-CeNP.

2. Materials and Methods

Materials

Chitosan (CS) with a degree of deacetylation of 75–85% and a low molecular weight (LMW, CAS Number: 448869); DP: 50-190 KDa (based on viscosity) and polyvinyl alcohol (PVA) with an approximate molecular weight of 60,000 (cat#8.43866) were obtained from Sigma-Aldrich, USA. Isopropanol, acetone, acetic acid, hexafluoroisopropanol (HFIP), ethanol, lithium bromide (LiBr), glutaraldehyde, Lysogeny broth (22) medium, and trypsin were supplied by Merck, Germany. The reagents 3-(4,5-dimethylthiazol-2-yl)-2,5-diphenyltetrazolium bromide (MTT) and dimethyl sulfoxide (DMSO) were also purchased from Sigma-Aldrich, USA. Sodium

carbonate (Na₂CO₃), a vitamin D3 assay kit, fetal bovine serum (FBS), and Dulbecco's Modified Eagle Medium (DMEM) were procured from DR. Mojallali (Iran), Ideal Diagnosing (Iran), Gibco (Waltham, MA, USA), and Lonza (Bornem, Belgium), respectively. SPL Life Sciences (South Korea) provided the 96-well and 12-well plates. Cerium oxide nanoparticles (CeO₂, 99.97%, 10–30 nm, CAS#:1306-38-3) were sourced from US Research Nanomaterials, Inc.

2.1. Extraction of silk fibroin

Silk fibroin (SF) was extracted from B. mori silkworm cocoons following Rockwood's protocol (23). In the first step, sericin protein was removed by degumming cocoons in 0.02 M Na₂CO₃ solution at 100 °C for 30 min. Then, they were rinsed in deionized water and, after drying, were dissolved in 9.3 M LiBr aqueous solution for 4 h at 60 °C. The resulting silk solution was dialyzed in distilled water to remove LiBr. At this point, to remove the insoluble particles, the silk solution was centrifuged at 4 °C. After completing these steps, the resulting silk solution was freeze-dried and stored at room temperature.

2.2. Extraction of collagen from rat tail

Rat tails were harvested from the post-experimental animals. The tails were processed following the protocol established by Rajan et al (24). In the initial stage of the process, the tails were washed entirely, and using a scalpel, the tendons were separated from the tails and washed with Phosphate-buffered saline (PBS) several times. Then, the samples were immersed in an acetone solution for 5 minutes, followed by immersion in a 70% isopropanol solution for an additional 5 minutes. After these steps, the samples were placed on a magnetic stirrer in a 0.02 N acetic acid solution at 4°C for 72 hours. Subsequently, the extracted collagen (22) was freeze-dried and stored in a freezer at minus 20°C for further use.

2.3. Surface modification of cerium oxide nanoparticles (CeNPs)

Fetal bovine serum (FBS) was utilized to modify and process the surface of cerium oxide nanoparticles (CeNPs). For this purpose, a 20% w/v CeNPs solution was prepared in FBS and magnetically stirred for 24 hours. The mixture was then left to dry completely at room temperature, preparing the CeNPs for further use. The surface charge of the FBS-modified CeNPs was determined using Zetasizer analysis (NANO-flex® II, Thermo Fisher Scientific, USA). For this analysis, 0.01 g of CeNPs were dispersed in absolute ethanol and homogenized for 10 minutes using a probe sonicator (Fisher Scientific, USA). Additionally, the CeNPscontaining solution was degassed in an ultrasonic bath for 5 minutes immediately before electrospinning.

2.4. Fabrication of nanofibrous scaffolds.

The polymer solution was prepared by dissolving various concentrations of extracted SF and Col (7%, 6%, 5%, 4%, and 3% w/v) in a weight ratio of 85:15 (SF: Col) using hexafluoroisopropanol (HFIP). The solution was stirred at room temperature and pressure. Additionally, the polyvinyl alcohol (PVA) and chitosan (CS) solution was prepared by dissolving 10% PVA in deionized water and 3% CS in 2% (w/v) acetic acid, maintaining a weight ratio of 80:20 (PVA: CS). For the electrospinning of SF-Col nanofibers, the prepared solution was loaded into a 5-ml syringe equipped with a 0.4 mm diameter needle. After process optimization, a high voltage of 14 kV was applied to the needle tip to create an electric field while a fluid jet was ejected at a rate of 1 ml/h, with fibers collected on a substrate positioned 15 cm from the syringe tip. For the electrospinning of PVA-CS nanofibers, a lower voltage of 8 kV was utilized, with the same ejection rate and distance.

2.5. Fabrication of nanofibers including vitamin D3 and CeNPs

In the first step, a 5% (w/v) SF solution was prepared in HFIP. Subsequently, 1%, 5%, 10%, and 20% (w/w) vitamin D3 were added to it (these ratios were selected based on the literature) (25). These solutions were magnetically stirred in closed bottles at room temperature for 12 hours. A 5% (w/v) Col solution was added to the SF solution in an 85:15 (SF: Col) weight ratio and then stirred for 12 h. The electrospinning was conducted at a flow rate of 1 mL/h, with a high voltage power supply set to 14 kV and a distance of 15 cm between the needle and the collector. Additionally, CeNPs were incorporated into a PVA-CS solution at varying concentrations (1%, 5%, and 10% w/w) relative to the total dry weight of PVA and CS used in solution preparation. For the PVA-CS-CeNP system, electrospinning conditions were optimized with a high voltage of 8 kV, a flow rate of 1 mL/h, and a distance of 15 cm from the syringe tip.

2.6. Cross-linking nanofibrous structure

Following electrospinning, all nanofibers were cross-linked using 0.5% (v/v) aqueous glutaraldehyde (GTA) vapor. A 10 mL aliquot of the 0.5% (v/v) GTA solution was placed in a Petri dish at the bottom of a desiccator, and the electrospun fibers were positioned on a porous ceramic shelf above the dish. After 12 hours of exposure, the fibers were removed from the desiccator and stored at room temperature.

2.7. Characterization of electrospun nanocomposites

The surface morphologies of the electrospun nanofibrous mats were evaluated using field-emission scanning electron microscopy (FESEM; MIRA3 TESCAN, Czech Republic) with an acceleration voltage of 10 kV at room temperature. The nanofibers were cut into appropriate

sizes and, before observation, were coated with 10 nm Au. The average fiber diameter of the fibers was calculated based on the processing of around 100 fibers in SEM images using Image J software (Image J, National Institutes of Health, Bethesda (NIH), USA).

Determining the chemical composition of the extracted SF and Col, powders of PVA and CS, and electrospun scaffolds was conducted using a conventional FTIR Spectrometer (NICO-LET IS10 FT-IR SPEC, Thermo Fisher, USA). The FTIR spectra analysis was performed over a range of 4000 to 400 cm⁻¹ at a spectral resolution of 4 cm⁻¹, with 16 scans.

A universal testing machine (UTM, SANTAM STM, Iran) was used to test the nanofiber mats' tensile strength, breaking elongation, and elastic modulus. Samples measuring 1×7 cm² were placed between the instrument's grips. The samples were stretched axially at a rate of 0.5 mm/min.

A video-based contact angle system (Adeeco, Iran) was used to measure the surface wettability of the nanofiber mats. Approximately 2 µL water droplets were applied to the dry surface of each sample using a micro syringe. The static contact angle was recorded over time, with five readings taken for each sample to ensure accuracy. The water uptake ratio for the fibrous mats was measured by total immersion in PBS (pH 7.4) at 37 °C. All samples (triplicates of each sample) of equal weight were collected after 24 h, and to remove the excess water, they were dried briefly using filter paper. All samples were weighed again, and the swelling capacity of the mats was calculated using the following equation (Eq. 1):

(Eq.1) Degree of swelling (%) = $(W_1 - W_0)/W_0 \times 100$

Where W_0 is the initial weight of the samples in the dry state, and W_1 is the wet weight after 24 h immersion in PBS. The weight changes of nanofiber mats (triplicates of each sample) at regular intervals (1, 4, 7, 14, 21, and 28 days) were performed by total immersion in PBS at 37 °C. The samples were removed from PBS and dried at predetermined times. The weight loss (%) was measured according to the following formula (Eq. 2):

(Eq.2) Weight Loss (%) =
$$(W_1 - W_0)/W_0 \times 100$$

Here, W_0 and W_1 are the dry weights of the nanofibers before and after immersion in PBS, respectively.

2.8. Vitamin D3 release

The vitamin D3 content of the fabricated nanofibers was evaluated using a vitamin D3 assay kit (Ideal Diagnosing, Iran). For this purpose, the nanofibers containing vitamin D3 of equal weight were transferred to an equal weight of 1% alcohol. Samples were incubated and shaken for 6, 21, 24, 48, 72, and 96 h at 37 °C. After the predetermined times, the medium was analyzed for vitamin D3 content according to the manufacturer's instructions for the vitamin D3 assay kit. Finally, absorption was measured at 450 and 630 nm using a microplate reader (Epoch, BioTec, USA).

2.9. CeNPs release

The release of CeNPs from nanofibers containing CeNPs was assessed by soaking nanofiber mats in PBS. At intervals of 1, 4, 7, 14, and 21 days, inductively coupled plasma atomic emission spectroscopy (ICP-AES, Spectro Arcos, Kleve, Germany) was applied to analyze changes in CeNPs concentrations in the CeNP-containing solutions.

2.10. Cytocompatibility assessment

Cell lines of mouse fibroblast (L929) were used to assess cell viability and the proliferation rates of nanofibers. Briefly, L929 cells were cultured in Dulbecco's Modified Eagle Medium (DMEM, Lonza, Bornem, Belgium) supplemented with 10% v/v FBS (Gibco, Waltham, MA, USA) and 1% v/v antibiotics (penicillin-streptomycin). The cells were incubated at 37 °C in an 85–95% humidified atmosphere containing 5% CO_2 . The medium was replaced every two days. Approximately 3×10^3 L929 cells were cultured in a 96-well plate (SPL Life Science, South Korea) and incubated at 37 °C for 24 h. Each side of the fibrous mat samples was sterilized by UV light in a biosafety cabinet for one hour. The nanofiber mats were added to each well of a 96-well plate, and after 24, 48, and 72 h of incubation, 10μ L of 3-(4,5-dimethylthiazol-2-yl)-2,5-diphenyltetrazolium bromide (MTT) solution (5 mg/mL in PBS) was added to each well. After incubation for four h, the media was replaced by 100 μ L of dimethyl sulfoxide (DMSO), and incubating continued for 20 min. Eventually, L929 cell proliferation was assessed via the OD values at 570 nm and 690 nm using a plate reader (Epoch, BioTek, US).

2.11. Cell adhesion

L929 Cell adhesion, proliferation, and morphological features on the nanofibrous membranes were observed after 3 days using FESEM. In brief, the L929 cells 2×10^4 were seeded on the nanofibrous mats and incubated for 3 days. After that, the mats were transferred to another well and fixed with 2.5% v/v GTA for 24 h, followed by rinsing with PBS twice. Subsequently, samples were dehydrated in a graded series of ethanol concentrations (30, 50, 70, 75, 80, 85, 90, 95, and 100%). Finally, fibrous mats were freeze-dried and surface-coated with gold, and observed by FESEM.

2.12. Cell migration (Scratch assay)

The human umbilical cord vein endothelial cells (HUVECs) were cultured in 12-well plates (2 × 10⁴ cells per well) at 37 °C. After 24 h, for the cell migration assay, the cell monolayer was scraped in a straight line using a 100 μL pipette tip. The UV-sterilized samples were transferred to the plates and incubated. After 24 hours, images were captured, and cell migration was analyzed using Image J software (National Institutes of Health, USA). These experiments were repeated 3 times.

2.13. In Vitro blood compatibility assay

The experimental procedure for blood collection and handling adhered to the Declaration of Helsinki and was approved by the Institutional Ethics Committee at MUMS, Iran (IR.MUMS.MEDICAL.REC.1400.453). A whole blood sample from a 30-year-old woman, anticoagulated with acid-citrate-dextrose, was added to 96-well plates with punched nanofibers and incubated at 37 °C for 2 hours. Samples were incubated at 37 °C for 2 hours. Blood samples for positive and negative controls were diluted in deionized water and normal saline, respectively. After centrifugation at 1500 rpm for 10 minutes, the absorbance of the clear supernatant was measured at 545 nm to quantify hemoglobin release due to red blood cell damage. Finally, the percentage of the hemolysis index was calculated using the following formula (Eq.3):

(Eq.3) Degree of Hemolysis (%) =
$$[(D_s - D_n) / (D_p - D_n)] \times 100$$

where Ds, Dp, and Dn indicate the measured absorbance values of the samples, the positive control, and the negative control, respectively.

2.14. Antibacterial assay

The antibacterial potential of fabricated nanofibers was investigated against Gram-negative *Pseudomonas aeruginosa* (*P. aeruginosa*) and Gram-positive *Staphylococcus aureus* (*S. aureus*). In this regard, the bacteria were incubated and shaken in a lysogeny broth (22) medium at 37 °C. After sterilization, the samples were added to LB medium and incubated and shaken at 37 °C for 24 h. The nanofibers-containing media were then added to the 1–5 ×10⁵ CFU/mL bacterial suspension and incubated and shaken at 37 °C for 24 h. Samples without nanofiber mats served as control groups. When these steps were completed, the supernatant absorbance was measured at 600 nm using a microplate reader (Epoch, Bio Tek, USA), and the antibacterial activity of samples was evaluated quantitatively as follows (Eq.4):

(Eq.4) Antibacterial Activity (%) =
$$[(D_s - D_n) / (D_p - D_n)] \times 100$$

Here, D_s , D_p , and D_n are the measured absorbance values of samples, the positive control, and the negative control, respectively.

2. 15. Induction of type 2 Diabetes in rats

All experimental protocols were approved by the Animal Ethics Committee of Mashhad University of Medical Sciences (IR.MUMS.MEDICAL.REC.1400.453). Male Wistar rats (8 weeks old, 200–230 g) were selected as the diabetic wound-healing model. The animals were housed under controlled conditions, maintaining a stable temperature of 22 ± 1 °C and a relative humidity of $55 \pm 5\%$, within a regulated air-conditioned environment. They were subjected to a 12-hour light/dark cycle and provided ad libitum access to a standard diet and tap water. For the Type 2 diabetic model, male rats were administered a high-fat diet (HFD) comprising 60% of calories from fat over 3 weeks. Then, they received a single intraperitoneal injection of

streptozotocin (STZ; Sigma-Aldrich, USA) at a dosage of 30 mg/kg of body weight in conjunction with the HFD throughout the experiment (26, 27). Three days following the STZ injection, blood samples were procured from the rats' tails to assess blood glucose levels utilizing a glucometer. Confirmation of the type 2 diabetic model was established when blood glucose levels exceeded 300 mg/dL. Furthermore, the rats' blood glucose levels were monitored daily, with insulin administration occurring only when glucose levels surpassed 500 mg/dL. The weights of the rats were meticulously documented, and due to the risk of polyuria, their bedding was changed more frequently.

2. 16. Induction of Diabetic Wound Healing Model

The rats were anesthetized with an intraperitoneal injection of ketamine (70 mg/kg) and xylazine (10 mg/kg). Once fully unconscious, the dorsal hair was shaved, and the skin was disinfected. Two full-thickness excisional wounds (8 mm in diameter) were created symmetrically on either side of the midline at the shoulder level using a sterile biopsy punch. A silicone splint was then carefully positioned over each wound and secured to the surrounding skin using 6-0 nylon sutures to minimize wound contraction and ensure consistent healing assessment.

2. 17. Treatment of Induced Diabetic Wound

The rats were systematically assigned to two distinct groups: (I) Type 2 diabetic wounds without treatment, and (28) Type 2 diabetic wounds receiving SF-Col-D/PVA-CS-CeNP nanofiber mat treatment. Following the creation of wounds, each rat was housed individually in separate cages. Subsequent to the administration of treatment, the wound sites were securely covered with bandages. Each group comprised 12 rats, and following the initial wound creation, each rat was confined to an individual cage.

2. 18. Macroscopic Diabetic Wound Healing Analysis

Wound healing was assessed based on both visual appearance and wound closure, with images captured using a Canon EOS 3000D (18MP) camera on days 0, 3, 7, 14, and 21 post-wounding. The percentage of wound closure was calculated to quantify the healing process and evaluate treatment efficacy using Equation 5:

(Eq.5) % Wound Closure=
$$(A_0 - A_n/A_0) \times 100$$

where A_0 represents the wound area on day 0, and A_n denotes the wound area at various time points (Days 3, 7, 14, and 21 post-operation).

2. 19. Histological study of wound healing

The rats were euthanized with an overdose of anesthesia at various time points (Days 3, 7, 14, and 21 post-wounding). The samples were removed with an 8 mm biopsy punch, which had the same diameter as the primary wound. The samples were fixed in 10% formalin, gradually dehydrated in ascending grades of alcohol, cleared in xylene, and embedded in paraffin. A microtome was then used to obtain five µm thin tissue sections, and the slices were stained with H&E following the manufacturer's protocol.

2. 20. Statistical Analysis

All statistical analyses were carried out using GraphPad Prism (v 9.0). Data analysis was performed using two-way ANOVA and Tukey's test. The t-test was performed to compare the mechanical data. A P-value of 0.05 was considered statistically significant, and all graphs were presented as mean \pm standard deviation (SD). All the experiments were repeated 3 times.

3. Results and discussion

3.1. Morphology and cytocompatibility assessment of electrospinning nanofibers

As illustrated in Fig. 1A-K, smooth, bead-free SF-Col nanofibers exhibiting uniform surface structures were observed across all concentrations. Further analysis established that the average diameters (n = 100) of SF-Col nanofibers at concentrations of 7%, 6%, 5%, 4%, and 3% (w/v) were 1956 ± 450 nm, 1257 ± 297 nm, 432 ± 142 nm, 271 ± 133 nm, and 168 ± 51 nm, respectively. This underscores the significance of polymer concentration in influencing nanofiber diameter. Previous research has indicated that polymer concentration directly affects nanofiber diameter (29, 30). Increased polymer concentrations enhance solution viscosity, thereby restricting stretching during the electrospinning process (31). Elevated polymer concentrations yield higher solution viscosity, which limits fiber elongation during electrospinning. This phenomenon occurs because highly viscous polymer solutions resist elongational forces, thereby constraining fiber thinning. However, it is imperative to optimize viscosity to prevent spinneret clogging and to ensure uniform fiber deposition. Additionally, solvent evaporation transpires more swiftly at heightened polymer concentrations, resulting in fibers with larger diameters (31). Wei et al. reported that SF nanofibers prepared in HFIP at a concentration of 8 wt% exhibited an average diameter of 1250 ± 410 nm (32). Furthermore, Antonios Keirouz et al. indicated that the diameter of SF: poly(glycerol sebacate) (PGS) (2:1) nanofibers surpassed 2 µm when 12% SF was dissolved in a solution of CaCl2 and formic acid (28). The SEM images of PVA-CS nanofibers displayed a smooth, bead-free structure characterized by randomly oriented fibers and a uniform surface, as depicted in Fig. 2A and B. The average diameter of the PVA-CS nanofibers (n = 100) was 211.4 ± 37.2 nm. Fig. 3A–I present SF-Col nanofibers incorporating vitamin D3 concentrations of 10%, 5%, 2%, and 1% (w/w), along with their average diameters. The average diameters (n = 100) for SF-Col-D3 nanofibers with vitamin D3 concentrations of 10%, 5%, 2%, and 1% (w/w) were 1361 \pm 433 nm, 1214 \pm 614 nm, 1155 \pm 474 nm, and 1087 \pm 475 nm,

respectively. In this study, we noted an increase in nanofiber diameter from 1087 ± 475 nm to 1361 ± 433 nm as the percentage of vitamin D3 increased. These values are consistent with prior studies. The presence of vitamin D3 may contribute to an increase in viscosity within the solution, potentially leading to the fabrication of fibers with larger diameters. This effect is attributable to the increased resistance to flow as vitamin D3 concentration escalates (25, 33). A study by W. Soo et al. concluded that elevating the vitamin D3 concentration from 6% to 20% resulted in an increase in nanofiber diameter from 324 ± 118 nm to 428 ± 129 nm (25). Furthermore, these findings further substantiate that vitamin D3 is effectively incorporated into the SF-Col fiber membrane.

Fig. 4A-F illustrate PVA-CS fibers containing 1, 5, and 10 CeNP (% v/v), along with their average diameters. The mean diameters of PVA-CS fibers with 1, 5, and 10 CeNP (% v/v) were recorded as 193 ± 92 nm, 279 ± 100 nm, and 221 ± 56 nm, respectively. Moreover, the average diameter of the PVA-CS nanofiber containing 10% surface-modified CeNP was 289.6 ± 59 . Fig. 5A-C depict the morphology of SF-Col-D/PVA-CS-CeNP fibers. The average diameter of this nanofiber (n = 100) was 621.4 ± 506 nm. The agglomeration of nanoparticles in polymer-matrix solutions is attributed to the significant magnetic attraction between the nanoparticles and the high surface energies resulting from a high surface area to volume ratio (34). The propensity of nanoparticles to aggregate limits their application in biological environments characterized by high ionic strength. Numerous protocols have been developed to effectively disperse nanoparticles, including dextran-coated CeNP, acid-coated CeNP (35), and non-ionic surfactant CeNP (34, 36). In the literature, nanoparticle aggregates exceeding four μ m are deemed biologically unacceptable due to their diminished surface area and potential to obstruct blood capillaries *in vivo*, leading to their subsequent clearance by the body's immune system (34). In

this study, we developed an innovative method for the surface modification of CeNP using FBS, as demonstrated in Figures 4 and 5, wherein a reduction in the size of CeNP aggregates was observed following surface modification with FBS. The modification of CeNP was confirmed by evaluating their zeta potential. Zeta potential values exhibited a significant decrease from -22 ± 3 (prior to surface modification) to -47 ± 4 (subsequent to surface modification), indicating a substantial alteration in the surface charge of the CeNPs. This reduction strongly implies successful surface modification with FBS, as the increased negative charge corresponds with the adsorption or interaction of negatively charged components from FBS onto the nanoparticle surface. Thus, we developed a surface modification technique utilizing FBS for CeNPs. Wang et al. stated that the aqueous stability of CeNPs can be significantly improved through surface modification with bovine serum albumin (BSA) as the major component of FBS through physical and chemical interactions. This process involves several key mechanisms, such as coating and stabilization, electrostatic interactions, hydrophilicity, and biocompatibility. BSA can effectively coat the surface of CeNPs. The protein molecules adsorb onto the nanoparticle surface, forming a protective layer that prevents agglomeration. This coating stabilizes the nanoparticles in aqueous solutions by providing steric hindrance, which reduces the likelihood of particles coming together and forming larger aggregates. About electrostatic interactions, BSA carries a net negative charge at physiological pH. This interaction contributes to the overall stability of the nanoparticles in solution by creating a repulsive force between particles, further preventing aggregation. Also, the modification with BSA, which is the main component of FBS, increases the hydrophilicity of CeNPs. The protein's hydrophilic nature enhances the solubility of the nanoparticles in aqueous media, making them more stable and less prone to settling or aggregation. On the other hand, FBS is a biocompatible protein that not only helps in stabilizing

CeNPs but also makes them suitable for biological applications. This biocompatibility is crucial when considering the use of these nanoparticles in drug delivery or biomedical applications (37). As shown in Figure 5A- C, the SEM images of the SF-Col-D/PVA-CS-CeNP scaffold revealed uniformly distributed fibers with a bead-free structure, random orientation, and interconnected porosity. The average diameter of the fabricated scaffold was 621.4 ± 50.6 nm. Furthermore, CeNPs, after surface modification, exhibit an almost uniform distribution and are well dispersed throughout the structure.

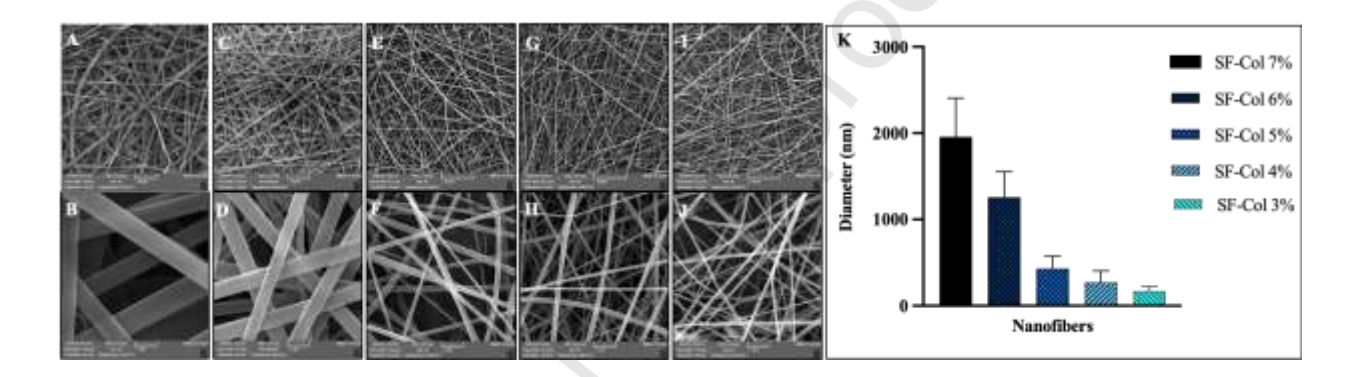


Fig 1. SEM images of (A, B) SF-Col 7%; (C, D) 6%; (E, F) 5%; (G, H) 4%; (I, J) 3%; and (K) diameter distributions of different concentrations of SF-Col nanofibers at the magnification values of (A, C, E, G, and I) 1500× and (B, D, F, H, and J) 10,000×.

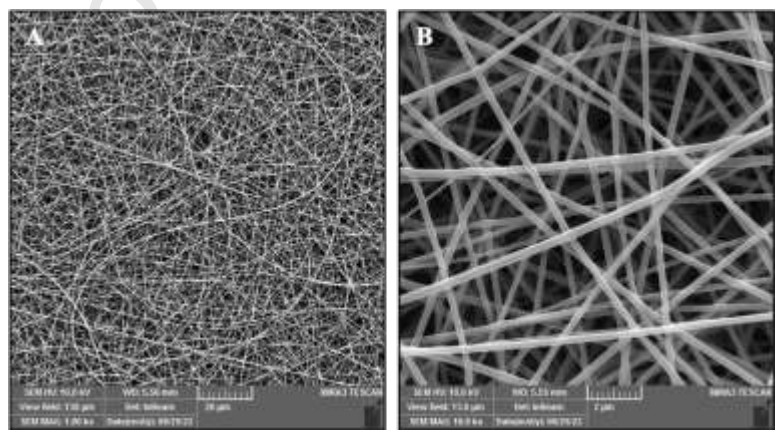


Fig 2. SEM images of PVA-CS nanofibers at the magnification value of (A) $1500 \times$ and (B) $1000 \times$.

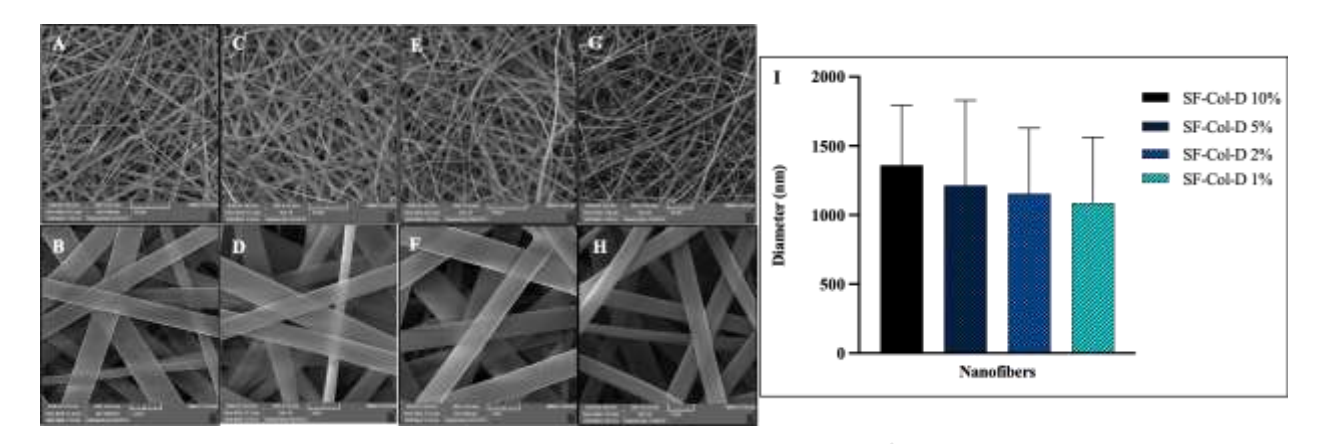


Fig 3. SEM images of SF-Col nanofibers with (A, B) D3 10%; (C, D) D3 5%; (E, F) D3 2%; (G, H) D3 1%; and (I) diameter distributions. The magnification values of A, C, E, and G were 1500× and B, D, F, and H were 12,000×.

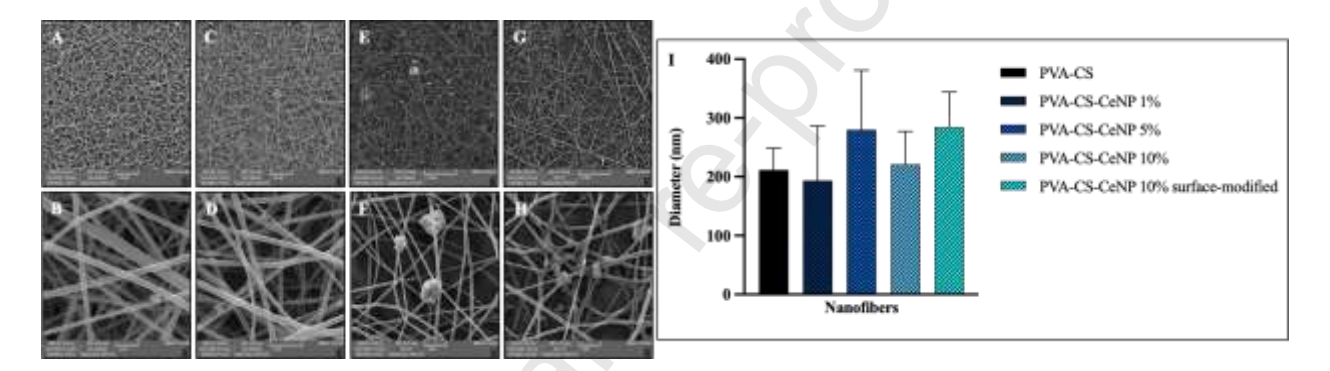


Fig 4. SEM images of PVA-CS nanofibers with (A, B) CeNP 1%; (C, D) CeNP 5%; (E, F) CeNP 10%; (G, H) surface-modified CeNP 10%; and (I) diameter distributions. The magnification values of A, C, E, and G were 1500×, and B, D, F, and H were 12,000×.

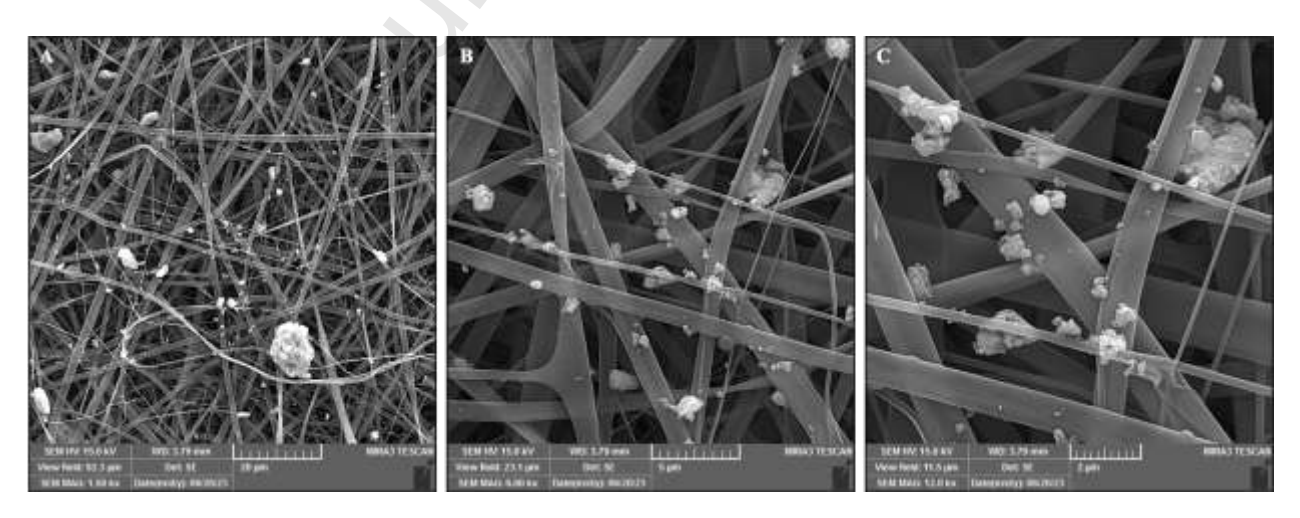


Fig 5. SEM images of (A, B, and C) SF-Col-D/PVA-CS-CeNP nanofibers. The magnification values of (A) was 1500×, (B) was 6000×, and (C) was 12,000×.

3. 2. Cytocompatibility test

In the first, we incorporated various percentages of vitamin D3 into SF-Col and CeNP within PVA-CS nanofibers. After examining the morphology of the fabricated nanofibers through SEM images, a cytocompatibility test was conducted on L929 cells to identify the optimal percentages of vitamin D3 and CeNP. As illustrated in Fig 6A, after 72 hours, cell viability was only 33.55 \pm 6 % and 33.71 \pm 5 % for the 10% and 5% vitamin D3 groups, respectively. In contrast, with lower vitamin D3 concentrations, cytotoxicity decreased, with cell viabilities of $70.49 \pm 7\%$ and $70.66 \pm 5\%$ for 2% and 1% vitamin D3, respectively. According to the obtained results, a 2% concentration of vitamin D3 was chosen to fabricate the electrospun nanofibers mats. Although CeNP did not reveal cytotoxicity effects in any percentages used for PVA-CS nanofibers, ultimately, 10% of CeNP was used in the SF-Col-D/PVA-Cs-CeNP nanofibers mats. As Fig. 6C exhibits, at different times, 2% vitamin D and 10% CeNP used in the final nanofiber membrane did not have more than 30% cytotoxicity on L929 cells. In a study by Wsoo et al., concentrations of 6%, 12%, and 20% vitamin D3 were used to fabricate electrospun cellulose acetate (CA) and ε-polycaprolactone (PCL) nanofibrous membrane; however, they didn't report the results of the cytotoxicity of scaffolds containing vitamin D3 (25). It seems we have succeeded in reaching an optimized percentage of vitamin D3 to fabricate a scaffold with acceptable cytocompatibility for wound healing applications.

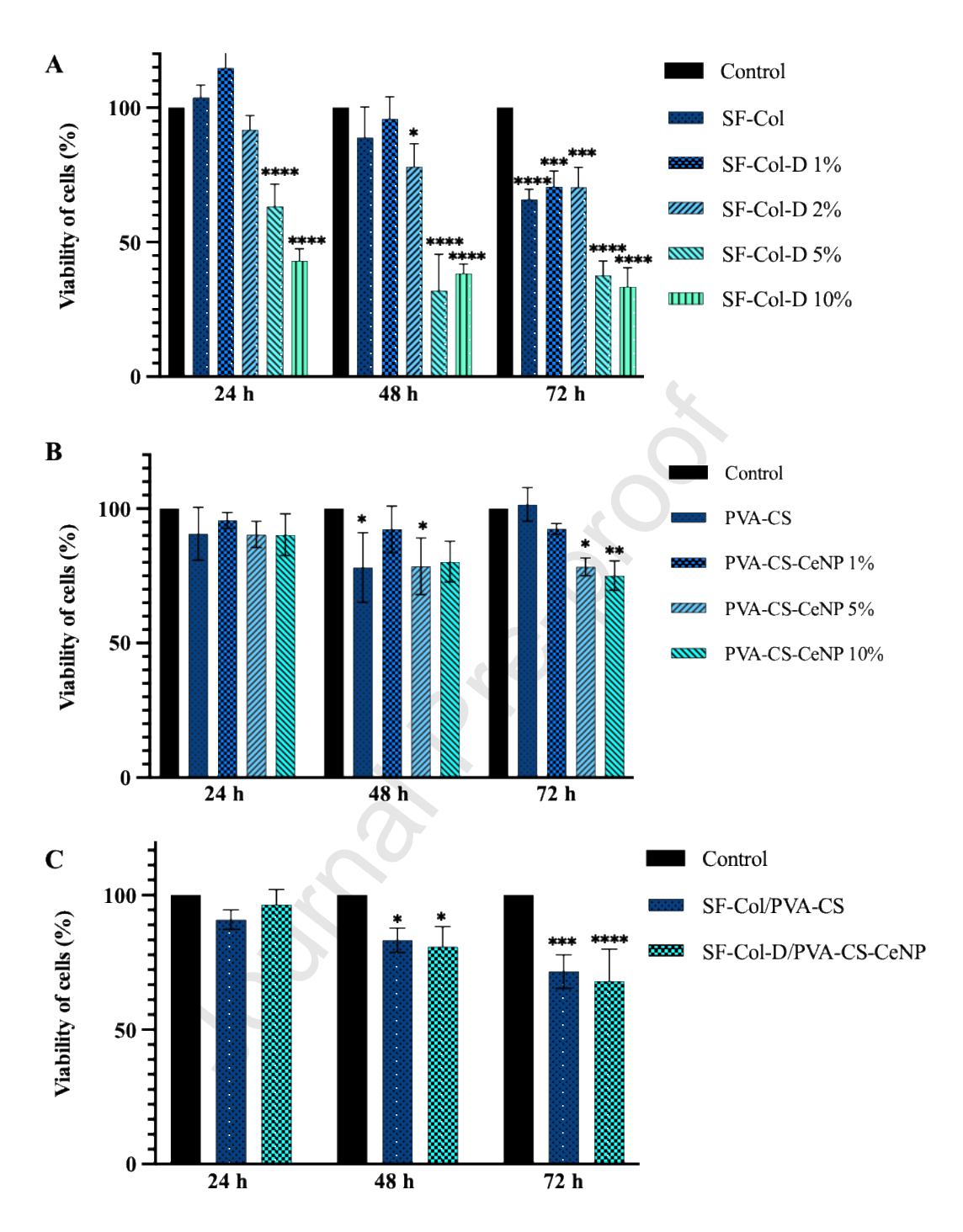


Fig 6. Cytotoxicity of different concentrations of (A) SF-Col-D; (B) PVA-CS-CeNP. (C) Cytotoxicity of SF-Col/PVA-CS and SF-Col-D/PVA-CS-CeNP nanofibers. The statistically significant differences were marked based on the p-values (*p \le 0.05, ** \le 0.01, *** \le 0.001, and **** \le 0.0001).

3. 3. FTIR Spectroscopy

Fig. 7A displayed the FTIR results of the extracted SF and Col. A broad peak in the 3416 cm⁻¹ band of the isolated SF's FTIR spectrum shows that the fibroin molecule contains amine functional groups. The peak at 1655 cm⁻¹, associated with the carboxyl group, further indicates the presence of functional groups in the SF structure. The stretching vibrations of the methylene (-CH₂) and methyl (-CH₃) groups within the SF structure are represented by the wave numbers in the 2930 cm⁻¹ and 1356 cm⁻¹ regions, respectively. Amine (-NH) groups, which are necessary for the structural integrity and biological activities of Col, are indicated by a broad peak in the region of 3328 cm⁻¹. The carbonyl (C=O) stretching, a crucial characteristic linked to the carboxyl functional groups in the Col polymer, is related to the peak at 1655 cm⁻¹. Additionally, the methylene (-CH₂) stretching vibrations within the Col structure are attributed to the peaks at approximately 2954 cm⁻¹. The intricacy of the Col and its several functional groups is further highlighted by the fact that peaks in the 1237 cm⁻¹ range correspond to the stretching vibrations of the carbon-nitrogen (C-N) and carbon-oxygen (C-O) bonds.

Additionally, the FTIR spectroscopy of PVA and CS polymers are illustrated in Fig. 7B. The broad peak observed at 3449 cm⁻¹ is associated with the stretching vibrations of O-H and N-H groups. The peak at 2872 cm⁻¹ corresponds to C-H stretching vibrations. The peak at 1659 cm⁻¹ indicates the presence of the amide group. Also, the spectrum of PVA displayed peaks associated with C-O stretching vibrations at 1096 cm⁻¹ and 1261 cm⁻¹, the asymmetric stretching vibration of the methylene group (CH2) at 2940 cm⁻¹, and a broad O-H stretching band at 3411 cm⁻¹. The band observed at 1735 cm⁻¹ is likely due to residual C=O stretching vibrations from polyvinyl acetate that remained after manufacturing.

As can be seen in Fig 7C, in the FTIR spectrum of non-cross-linked SF-Col nanofibers, a broad peak in the region of 3309 cm⁻¹ is observed, indicating the presence of free amine (-NH) and hydroxyl (-OH) groups. This peak demonstrates that both SF and Col retain significant amounts of unreacted functional groups, which can engage in hydrogen bonding and contribute to the hydrophilicity of the fibers. Conversely, in the spectrum of cross-linked SF-Col nanofibers, the intensity of this peak often reduces, indicating that many of these functional groups have participated in covalent bonding due to cross-linking with GTA. In cross-linked SF-Col nanofibers, the Amide I peak may shift to lower wavenumbers, suggesting a change in the secondary structure of the fibers, such as an increased stabilization of β-sheet conformations. Additionally, the Amide II peak, which corresponds to N-H bending vibrations, may also exhibit changes in intensity or position between the two spectra. In cross-linked samples, a greater intensity of the Amide II peak could indicate an increased number of N-H bonds formed due to cross-linking, further reflecting the alteration of the fiber's chemical structure. In the 1000–1300 cm⁻¹ region, characteristic peaks related to C-N and C-O stretching can be analyzed to differentiate the cross-linked fibers from the non-cross-linked ones. The presence of new peaks in the cross-linked spectrum indicates the incorporation of GTA, which introduces additional C-O and C-N linkages, confirming successful cross-linking. Our results represented the characteristic bands of SF and Col, especially the characteristic bands of Silk I (1655 cm⁻¹ and 1541 cm⁻¹ band) and collagen amides A, B, I, II, and III, which support the results of Ling et al. (38) and Zhang et al. (39).

The FTIR spectrum of non-cross-linked PVA-CS nanofibers exhibits a broad absorption peak around 3401 cm⁻¹, attributed to hydroxyl (-OH) groups from PVA and CS and amino (-NH) groups from CS, indicative of strong hydrogen bonding interactions. These interactions enhance

the fibers' hydrophilicity and moisture retention properties. Upon cross-linking, the intensity of this peak decreases, reflecting the involvement of -OH and -NH groups in covalent bonding, reducing hydrogen bonding and potentially altering hydrophilicity. The Amide I band (~1735 cm⁻¹), associated with C=O stretching in CS, may shift to lower wavenumbers in cross-linked fibers, signifying structural changes in CS. Similarly, alterations in the Amide II band, associated with N-H bending, point to cross-linking-induced modification in N-H bonding. New interactions between PVA and CS are shown by additional peaks in the 1000-1300 cm⁻¹ range that correspond to C-N and C-O stretching. The structural changes and molecular interactions resulting from cross-linking have been confirmed by other characteristic peaks, including 3310 cm⁻¹ (-OH), 2930 cm⁻¹ (C-H), and 1728 cm⁻¹ (C=O). The FTIR spectrum of uncross-linked SF-Col/PVA-CS nanofibers shows firm peaks around 3400 cm⁻¹, related to -OH and -NH groups, indicating hydrogen bonding and hydrophilicity. Cross-linking reduces the intensity of these peaks, reflecting covalent bonding between functional groups, which alters hydrophilicity. Characteristic Amide I and II bands in SF-Col fibers (1730 cm⁻¹ and ~1550 cm⁻¹) and C-N/C-O stretching peaks (1000–1300 cm⁻¹) in PVA-CS fibers exhibit shifts or intensity changes post cross-linking, signifying structural modifications.

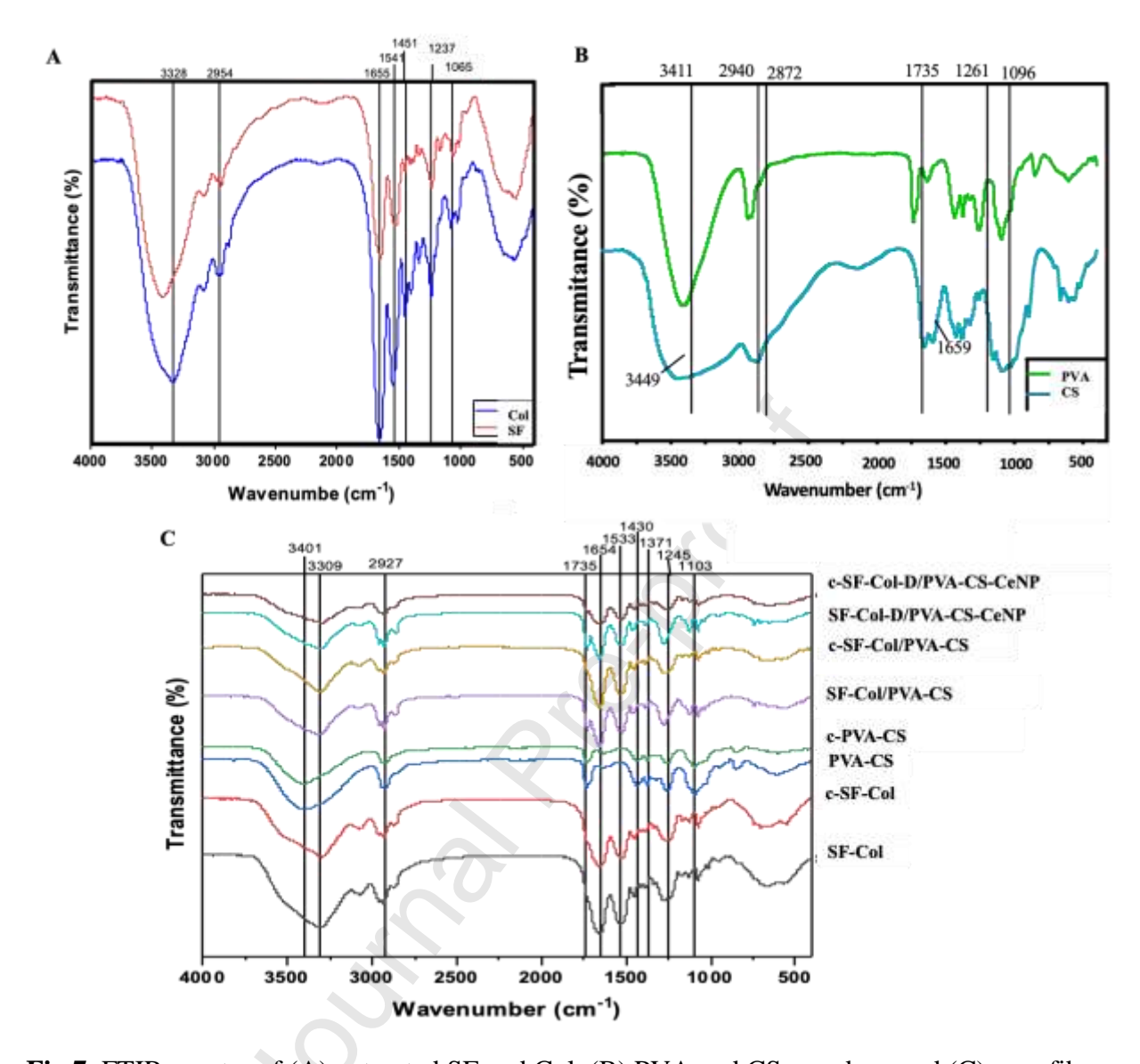


Fig 7. FTIR spectra of (A) extracted SF and Col, (B) PVA and CS powders, and (C) nanofiber

3. 4. Mechanical Properties of the Electrospun Nanofibers

The tensile strength and strain of SF-Col nanofibers are 0.38 MPa and 15.34%, respectively, according to their mechanical characteristics. Cross-linking improves structural stability and lowers strain by increasing tensile strength and decreasing deformation. Cross-linked fibers provide better resistance to degradation and increased biostability, while uncross-linked fibers exhibit more flexibility. Cross-linking is a chemical process that forms covalent bonds between

polymer chains, enhancing structural stability and resistance to degradation. This process involves multifunctional cross-linking agents that react with specific functional groups within the polymer network, restricting chain mobility. As a result, while cross-linked fibers exhibit superior biostability and mechanical strength, they lose the flexibility observed in uncross-linked fibers. This reduction in flexibility occurs because the formation of chemical bonds between polymer chains limits their ability to slide past one another, creating a rigid, interconnected network. In this study, polyvinyl alcohol (PVA) was cross-linked via the reaction between its hydroxyl groups and the aldehyde groups of glutaraldehyde; in contrast, chitosan was crosslinked through interactions between its amino groups and glutaraldehyde's aldehyde groups. Additionally, strong hydrogen bonding between chitosan and PVA further reinforced intermolecular interactions, contributing to reduced chain mobility. Concurrently, glutaraldehyde may also interact with silk fibroin and collagen, further integrating the polymer matrix and preventing molecular rearrangement. These combined interactions lead to a more stable yet less flexible fiber structure, which is essential for applications requiring durability and controlled degradation.

Increased stiffness and durability are indicated by a shift in the stress-strain curve for cross-linked fibers, which shows higher stress at yield and lower strain at breaking. The addition of CeNP and Vitamin D3 to SF-Col-D/PVA-CS-CeNP nanofibers improves their mechanical performance and overall tensile strength (1.21 MPa and 3.90 MPa and strain 8.43% and 1.800% for SF-Col-D/PVA-CS-CeNP and c-SF-Col-D/PVA-CS-CeNP, respectively).

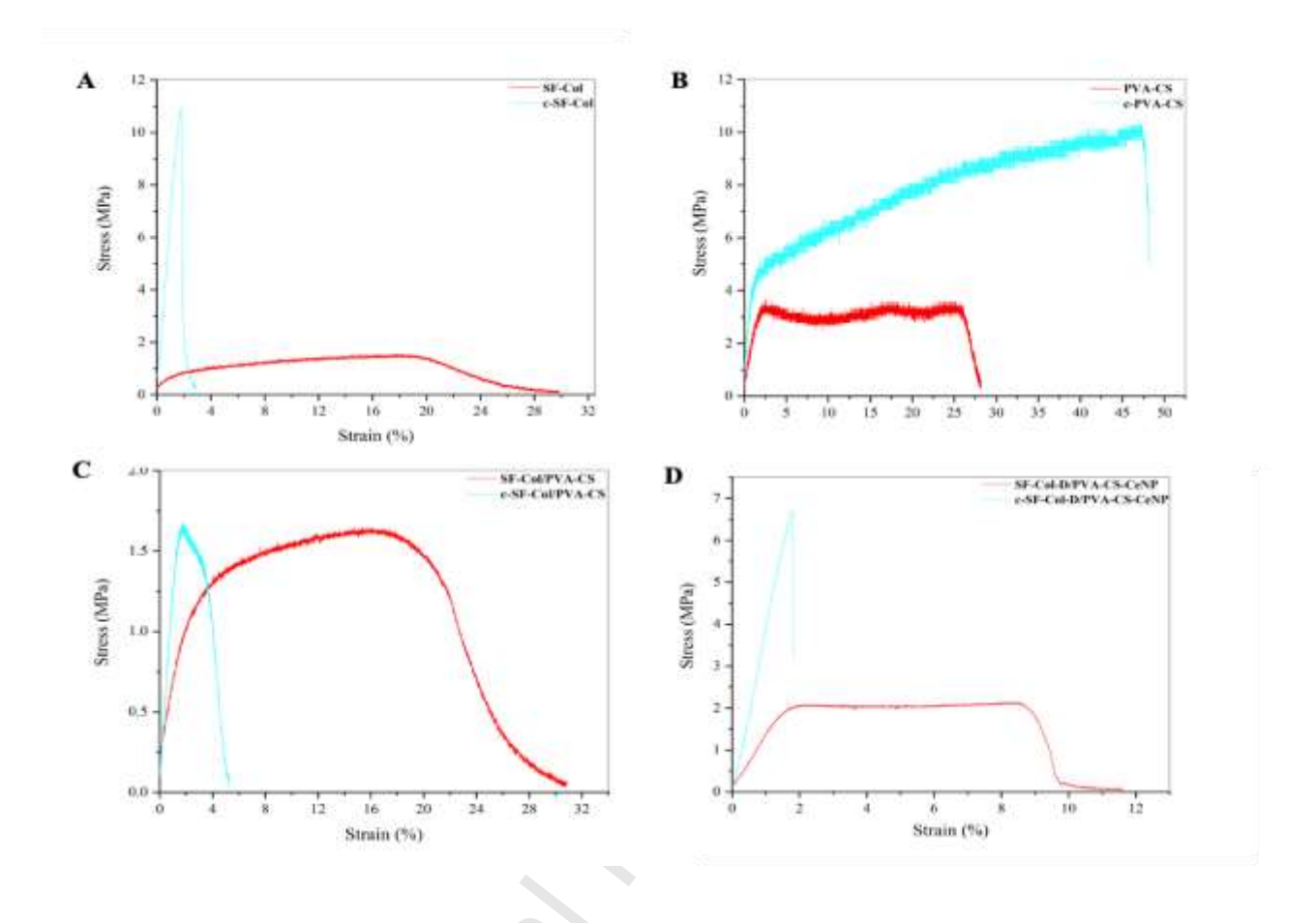


Fig 8. Stress-strain curves of (A) SF-Col and cSF-Col; (B) PVA-CS and cPVA-CS; (C) SF-Col/PVA-CS and cSF-Col/PVA-CS; and (D) SF-Col-D/PVA-CS-CeNP and c-SF-Col-D/PVA-CS-CeNP nanofibers.

Table 1. Mechanical Properties of Nanofibrous Membranes.

Nanofibers	Stress (40)	Elongation (%)	Module (40)
SF-Col	1.65	15/34	0.38
c-SF-Col	10.95	1.78	6.57
PVA-CS	0.69	24.8	1.63
c-PVA/CS	1.25	47.27	2.39
SF-Col/PVA-CS	1.57	17.79	0.43
c-SF-Col/PVA-CS	0.14	1.49	1.03
SF-Col-D/PVA-CS-CeNP	2.13	8.43	1.21
c-SF-Col-D/PVA-CS-CeNP	6.71	1.800	3.90

3. 5. Contact Angle

A nanofibrous scaffold's balance between hydrophilicity and hydrophobicity significantly influences cell adhesion and proliferation on its surface (41). The contact angle measurements for the nanofibers at the third and sixth seconds are shown in Fig. 9A and B. Notably, the PVA/CS nanofibers exhibit the lowest contact angle, indicating high hydrophilicity. Following cross-linking, all nanofiber mats show a slight increase in contact angle. Integrating natural polymers with synthetic hydrophobic polymers can effectively reduce the contact angle of the fiber mats, further enhancing the hydrophilicity of the fabricated nanofibers. Nanofibers containing SF and Col display impressive hydrophilic properties due to their high content of amino and carboxylic groups. In our investigation, we assessed the contact angles of SF-Col nanofibers prior to and subsequent to the cross-linking process. Three seconds after applying a droplet, the measured contact angles were 35° and 60° before and after the cross-linking,

respectively. Furthermore, 6 seconds after droplet application, the contact angles recorded were 35° and 53° before and after cross-linking, respectively. In comparison, a study by Mohammadzadeh Moghadam et al. reported contact angles of $75.31^{\circ} \pm 7.5$ for SF nanofibers and $69.94^{\circ} \pm 7.68$ for gelatin-SF (30:70) nanofibers (42).

Due to the abundance of hydrophilic groups in PVA (OH) and CS (NH₂ and COOH), both polymers are inherently hydrophilic and exhibit a high affinity for water molecules, enhancing the moisture absorption capacity of nanofibers (43). In a study by Cheng et al., the water contact angles for PVA, CS, and PVA/CS/erythromycin nanofiber membranes were reported as 20.16°, 21.02°, and 30.56°, respectively. They noted that adding CS to PVA nanofiber mats increased the water contact angle (43). In this study, cross-linking enhanced the water contact angle of the fabricated nanofibers, as shown in Fig. 9. Also, the results show that loading vitamin D3 and CeNP into structures increased the contact angle before cross-linking. However, this effect was not observed after cross-linking. During the wound healing process, an optimal contact angle in scaffolds can improve the absorption of secretions. For fibroblast cell adhesion, the ideal water contact angle has been reported to range between 55° and 75° (32). The contact angle of fabricated SF-Col-D/PVA-CS-CeNP nanofiber mats was in the same range before and after cross-linking

3. 6. Swelling and Weight Loss

The ability of biomaterials to absorb water is crucial for preventing the loss of body fluids and nutrients following transplantation (44). Generally, a higher swelling percentage after soaking results in more significant deformation and reduced stability. In this study, Col and PVA were identified as hydrophilic polymers, contributing to increased water absorption. Additionally, CS

(45) is particularly valued as a wound dressing material due to its favorable swelling properties, which help maintain structural integrity while supporting moisture retention (46). Also, in a study, the inflation rate of SF was 405% (42). The recorded water absorption (swelling) percentages for SF-Col, PVA-CS, SF-Col/PVA-CS, and SF-Col-D/PVA-CS-CeNP nanofibers were $436 \pm 16\%$, $262 \pm 8\%$, $381.5 \pm 11\%$, and $379.5 \pm 6\%$, respectively (Fig. 9C).

The most remarkable finding is that in our study, the highest amount of swelling was in the SF-Col scaffold with the amount of 16.5436±16.5, which had the highest amount of Col among the nanofibers (Fig. 9C). In a study, it was stated that the swelling percentage of SF-Col II composite membrane decreases with the decrease of type II collagen percentage (46). Rigel Antonio Olvera Berna et al. reported that swelling increases slightly with CS content in CS/PVA nanofibers (47).

The degradability of materials produces fragments that can be removed from the location (but not necessarily from the body) by fluid transport (48). The degradation of nanofibers is related to various properties, such as solvent type and concentration of polymer. Fig. 9D shows the weight loss of nanofibers after 1, 4, 7, 14, 21, and 28 days of immersion in PBS. The weight loss values after 28 days of SF-Col, SF-Col/PVA-CS, and SF-Col-D/PVA-CS-CeNP nanofibers were 25.6±2, 35.6±2, and 35.7±2, respectively. The results demonstrated that higher polymer concentration reduces the degradability of nanofibers (49). The lowest rate of degradation was observed in SF-Col nanofibers, and with the addition of PVA-CS, the rate of degradation increased at all times. Also, the noteworthy aspect is that it seems the addition of vitamin D3 and CeNP does not significantly affect nanofiber degradation or stability. Conversely, higher swelling percentages in the nanofibers lead to reduced material stability (46). Xiang-Long Lin et

al. stated that after 21 days, type II collagen degraded due to a very high swelling capacity, and SF powder appeared around the Col II-SF composite membrane (46).

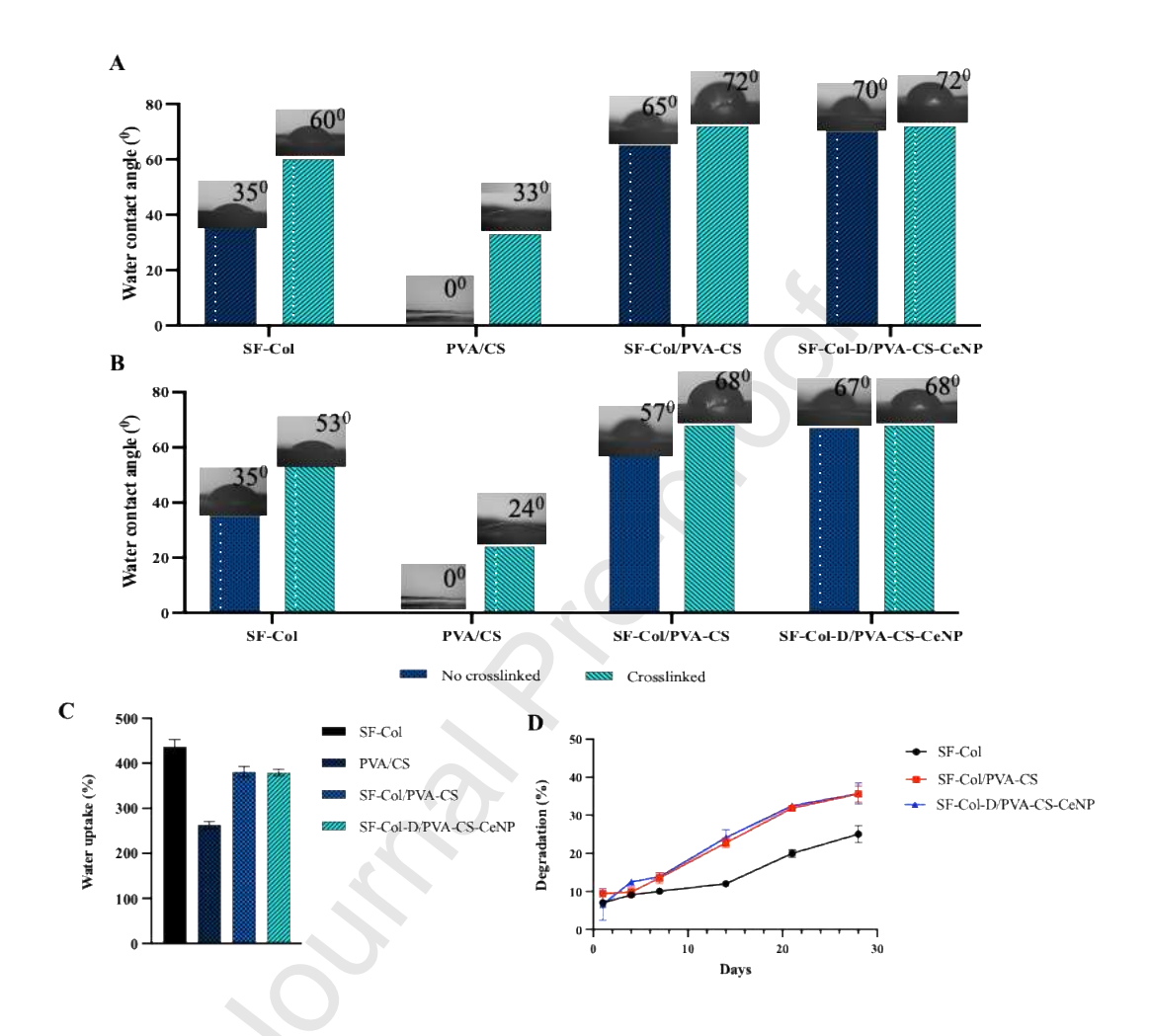


Fig 9. Contact angle of nanofibers (A) in the third and (B) in the sixth seconds after contact of water drop before and after cross-link; (C) swelling properties of SF-Col, PVA-CS, SF-Col/PVA-CS, and SF-Col-D/PVA-CS-CeNP electrospun nanofibers after 24 h immersion in PBS; (D) the weight loss of SF-Col, SF-Col/PVA-CS, and SF-Col-D/PVA-CS-CeNP nanofibers after 1, 4, 7, 14, 21, and 28 days of incubation in PBS. Data are shown as mean ± SD, n=3.

3. 7. Vitamin D3 release

An essential requirement for successful in vivo scaffolds is the sustained release of drugs over time. To the best of our knowledge, this work represents the first attempt to design SF-Col nanofibers as a drug delivery system (DDS) specifically for vitamin D3. The measured concentrations of vitamin D3 after immersion in 1% alcohol for 6, 12, 24, 48, 72, and 96 hours were 52 ± 3.1 , 67 ± 9.2 , 72 ± 0.96 , 71 ± 72.3 , 72 ± 1.48 , and $72.38 \pm \mu g/mL$, respectively (Fig. 10A). Our results indicate that the maximum release of vitamin D3 from the nanofibers, reaching $72.10 \pm 0.96 \mu g/mL$, occurred within 24 hours. A combination of hydrophobic and hydrophilic properties likely enables a steady, sustained release of vitamin D3 over time (25). Xiaoyue Sheng et al. fabricated Vitamin E-loaded SF nanofibrous mats with a sustained release of vitamins for skin care tissue regeneration (50). A sustained release of vitamins was observed from the loaded A and E fibers, extending over approximately 60 hours (51). In our study, vitamin D3-loaded nanofibers demonstrated not only an optimal morphology in SEM images but also a favorable vitamin release profile. Given the critical role of vitamin D3 in promoting keratinocyte proliferation, its sustained release significantly contributes to enhancing the wound healing process.

3. 8. CeNP release

Fig. 10B exhibits the release profile of CeNPs from SF-Col-D/PVA-CS-CeNP structures over predetermined time intervals. The results demonstrate that the maximum release occurs within the first 24 hours, after which the release stabilizes and remains relatively consistent for up to 21 days. The size of CeNPs was 10–30 nm, and the highest release rate was observed during the initial 24 h of immersion in PBS. The initial decrease in CeNP release, followed by a gradual increase, can be explained by several factors. Initially, a burst release occurs due to the high concentration of CeNPs located on the surface of the nanofibers. This is further facilitated by the rapid diffusion of liquid into the nanoparticle-rich surface area, the hydrophilic nature of the

fibers, their high surface area-to-volume ratio, and their porous structure. These factors together accelerate the release of CeNPs, particularly those not encapsulated within the fiber core but located at the fiber edges. After the initial burst release, the release rate decreases as the nanoparticles are adsorbed onto the fiber surface or the surrounding medium. The release then gradually increases as the nanoparticles undergo a controlled desorption process. This transition is followed by a slower, diffusion-controlled release phase during the later stages. These observations are consistent with the trend shown in Fig. 10B and align with the expected release profile based on the nanoparticle behavior and fiber structure. A study by Ahmad Rather et al. explored PCL-gelatin nanofibers containing CeNPs for wound healing applications, highlighting that the hydrophilic nature of the nanofibers enhanced CeNP release, thereby increasing their therapeutic efficacy (52). The activity of reactive oxygen species (ROS), highly reactive molecules that contribute to exacerbating skin inflammation, has been reported to be decreased by CeNPs. During the initial stages of wound healing, ROS levels typically surge, and the burst release of CeNPs within the first 24 h effectively reduces ROS production. This reduction decreases inflammation and accelerates the wound healing process. It has been reported that one of the mechanisms of CeNPs in the body is their ability to simulate the function of superoxide dismutase (SOD), playing a crucial role in mitigating oxidative stress (53). Superoxide anions, as one of the primary ROS generated in the body, are neutralized by SOD activity (53). SOD-like activity and release of CeNPs from PCL-Gelatin nanofibers were investigated by Hilal Ahmad Rather et al (52). In a related paper, PCL-gelatin nanofibers were immersed in Tris buffer and PBS for various durations (30 minutes, 24, 48, and 96 hours). The results showed that faster nanofiber degradation led to the rapid release of CeNPs, with sustained release continuing for up

to 96 hours. In this paper, within the first 24 hours of immersion in PBS, the highest release of CeNPs from nanofibers was observed.

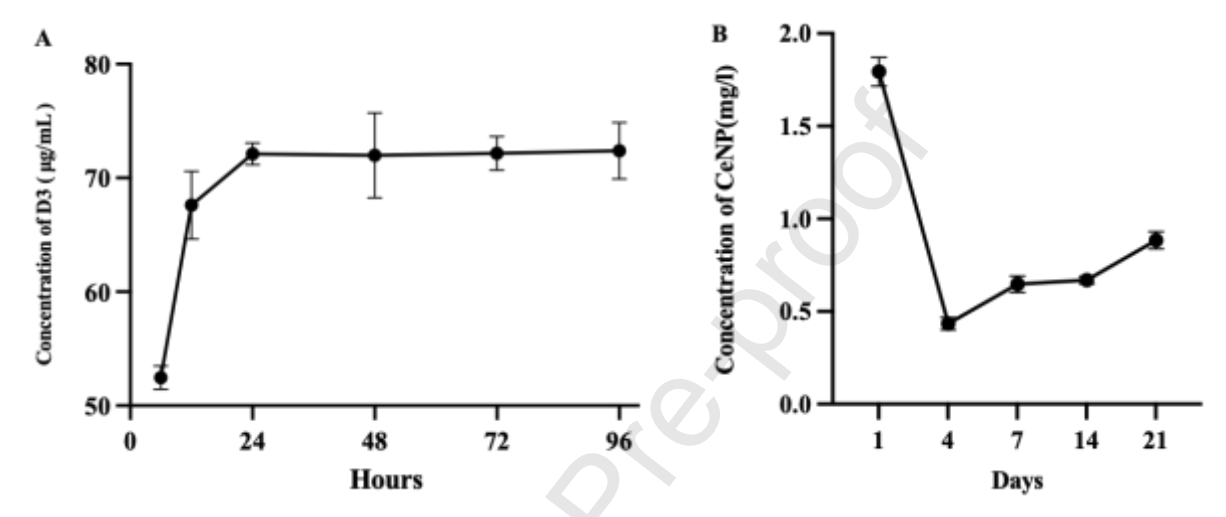


Fig 10. Release properties of (A) vitamin D3 from nanofibers prepared after 6, 12, 24, 48, 72, and 96h immersion in 1% alcohol; (B) CeNP release from SF-Col-D/PVA-CS-CeNP nanofibers after 1, 4, 7, 14 and 21 days. Data are shown as mean ± SD, n=3.

3. 9. Cell Adhesion and Migration

Considering the role of fibroblasts in the wound healing process (54), we investigated the adhesion of fibroblast cells (L929) on the surface of nanofiber membranes. In the wound healing process, the smooth surface of nanofibers is a critical parameter to facilitate cell attachment and proliferation. Changes in the surface energy of the nanofiber membrane predominantly control cell adhesion. Hydrophilic surfaces with higher energy promote adhesion, whereas lower energy substrates usually inhibit cell adhesion (55). Relatively hydrophilic/hydrophobic surfaces are desirable for the adsorption of surface proteins that mediate cell adhesion and provide downstream signals to specific cell adhesion receptors. These proteins cause the deposition of

ECM components essential for tissue remodeling (55, 56). SEM images showed that cultured cells adhered to, proliferated on, and extended across the surface of the nanofibers (Fig. 11A and B). The polygonal shape of the fibroblasts was observed, which indicates healthy cells. This demonstrates excellent interaction between the adhered cells and the fabricated structures. The optimal ratio of natural and synthetic polymers, appropriate solvents, cross-linkers, and precise cross-linking times led to high-quality nanofibers suitable for application as wound dressing. As evident in the SEM images, fibroblasts were well attached and proliferated on the surface of the SF-Col-D/PVA-CS-CeNP nanofibers. In the study by Minlie Yang et al., it was reported that cell adhesion and proliferation were significantly enhanced by the three-layer Col-SF-BG (bioactive glass) composite (57). Additionally, in skin wound healing, cell migration plays a crucial role alongside cell adhesion. The impact of the fabricated nanofibers on the migration of HUVEC cells was evaluated using the scratch test under in vitro conditions. As shown in Fig. 11E and F, the migration of HUVEC cells exposed to electrospun nanofibers was significantly enhanced by the SF-Col-D/PVA-CS-CeNP nanofibers compared to the control group (P < 0.05).

3. 10. In Vitro Blood Compatibility Assay

Hemolysis occurs when the osmotic pressure inside red blood cells (RBCs) increases, leading to cell rupture and the release of hemoglobin. The hemolysis percentage is a critical measure for evaluating the biocompatibility of nanofiber scaffolds. According to the ASTM F756-00 standard (Standard Practice for Assessment of Hemolytic Properties of Materials), materials are categorized based on their hemolytic index: materials with a hemolysis percentage more significant than 5% are considered hemolytic, those between 5% and 2% are slightly hemolytic, and those with less than 2% are classified as non-hemolytic (43). An implant with enhanced thromboresistance and minimized plasma protein adsorption can be applied successfully in the

Journal Pre-proof

clinic (58). The blood compatibility results of the nanofiber mats indicated that, compared to the positive control (distilled water), the nanofibers had no significant adverse effects on hemolysis. The hemolysis percentages for SF-Col, PVA/CS, SF-Col/PVA-CS, and SF-Col-D/PVA-CS-CeNP were 0.12 ± 0.1 , 0.51 ± 0.39 , 0.40 ± 0.24 , and 0.16 ± 0.15 , respectively. (Fig. 11G). In our study, the hemolysis percentage of all fabricated nanofibers was less than 2% and non-hemolytic. Cheng et al. reported a hemolysis percentage of less than 2% for PVA/CS erythromycin nanofibers (43). Also, Jie Qi et al. reported PVA hemolysis percentages of 1.6%(59). Fiber diameters, energy, roughness, wettability, and surface tension of nanofibers can affect the blood compatibility of nanofibers (60). The nanofibers with small fiber diameters (61) and hydrophilic properties (62) exhibited better blood compatibility.

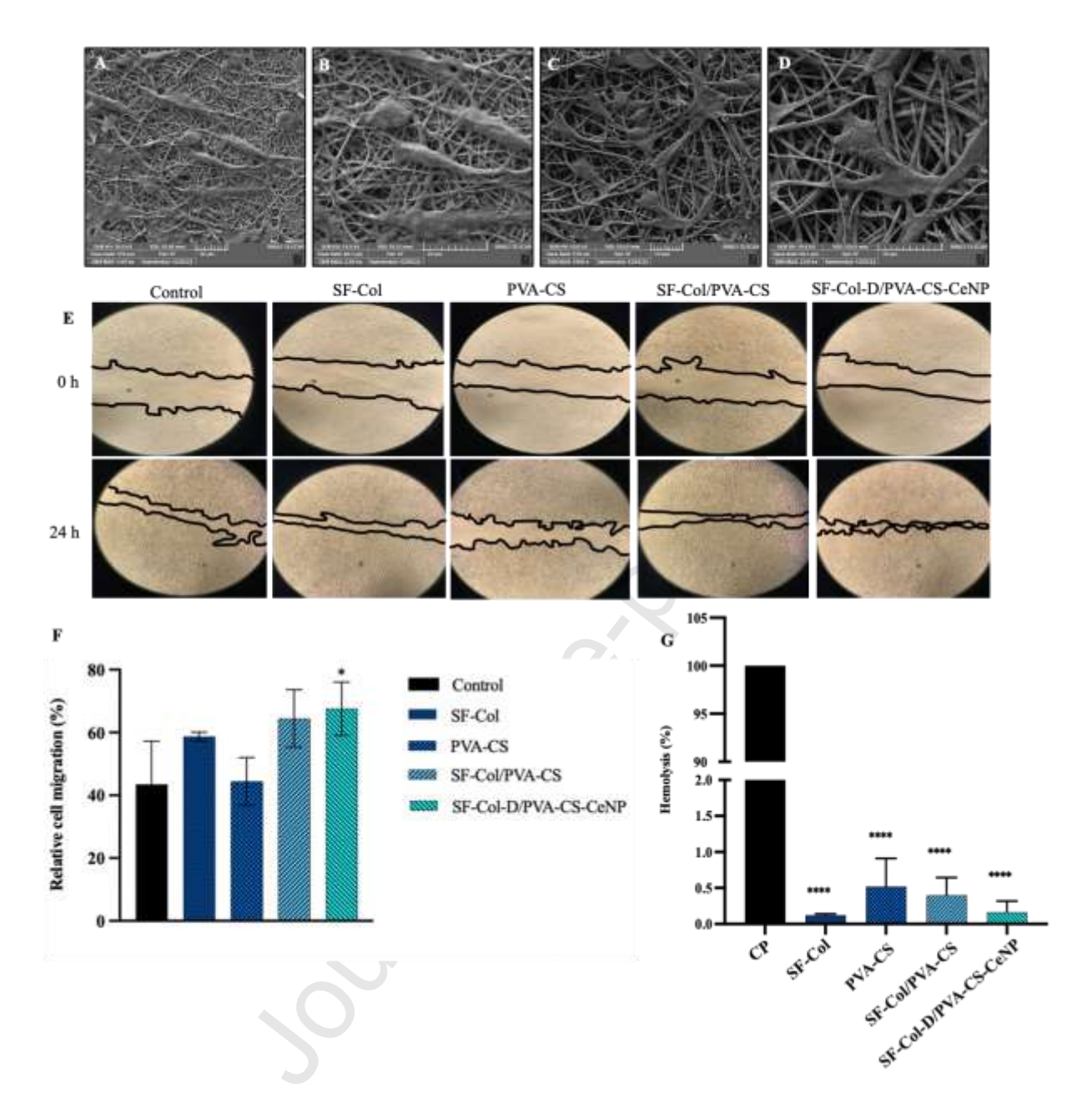


Fig. 11. FESEM image of L929 cell attachment on the surface of (A and B) SF-Col/PVA-CS; (C and D) SF-Col-D/PVA-CS-CeNP nanofiber membranes; (E) the migration of HUVEC cells after treatment by nanofiber mats at zero hours (before the start of treatment) and 24 hours after treatment (in the microscopic images, the progressive edges are marked by black color); (F) HUVEC migration percentage after 24 hours. Data are shown in comparison with the control, as mean ± SD, and *P≤0.05, n=3; (G) hemolysis percentage of SF-Col, PVA/CS, SF-Col/PVA-CS, and SF-Col-D/PVA-CS-CeNP nanofibers. Data are shown in comparison with the positive control and as mean ± SD and ****P<0.0001.

3. 11. Bacterial Penetration Activity

The data analysis showed that the *Staphylococcus aureus bacteria* treated by SF-Col/PVA-CS and SF-Col-D/PVA-CS-CeNP nanofiber mats had lower survival than the control group (P≤0.05) (Fig. 12A and B). Also, the survival of *Pseudomonas aeruginosa bacteria* treated by SF-Col-D/PVA-CS-CeNP significantly decreased compared to the control group (P<0.05). Considering the high risk of infection, especially in chronic wounds such as diabetic wounds (63), an antibacterial agent in the wound dressing can be promising for healing the wound. In the literature, CS has been proven to have antibacterial properties (64, 65). The antibacterial effects of SF-Col/PVA-CS membrane can result from electrostatic interactions between amine groups of CS with the surface negative charge of bacteria (66). Santiago-Morales et al. reported that PAA/PVA membranes significantly decreased the growth of bacteria *S. aureus* and *E. coli* (67).

Additionally, nanoparticles can have long-term antibacterial effects and low toxicity compared to conventional antibiotics (68). It is reported that the antibacterial properties of CeNP with a size of less than 54 nm have been proven (69). CeNP has a unique antibacterial capacity based on the reversible conversion between two valence states of Ce³⁺ and Ce⁴⁺ (69). A surface coating, in addition to increasing the dispersibility in an aqueous environment and advancing the biocompatibility of CeNP, can also enhance its antibacterial properties. In previous studies, dextran-coated CeO₂ NPs, acid-coated CeO₂ NPs (35), and a non-ionic surfactant (36) exhibited strong antibacterial effects on *P. aeruginosa* and *E. coli bacteria*, respectively. In our study, FBS-coated CeNPs loaded into PVA-CS nanofibers demonstrated significant antibacterial effects (Fig. 12A and B). The primary antibacterial mechanism of CeNP is believed to stem from its direct interaction with bacterial cell membranes(21). The minimal difference in antibacterial activity between the nanofiber groups with and without CeNPs could be attributed to several

factors. First, the type of bacteria used in the assay may influence the antibacterial effectiveness of CeNPs. Additionally, the antibacterial properties of CeNPs can vary depending on the oxidation state of cerium (Ce⁴⁺ vs. Ce³⁺), which can affect their bioactivity. Another potential factor is the non-uniform distribution of the CeNPs within the nanofiber matrix, which could result in an uneven release and, consequently, a less pronounced antibacterial effect. However, as shown in Fig. 12, the group containing CeNPs still demonstrates a statistically significant difference in antibacterial activity against both Gram-positive and Gram-negative bacterial strains. This suggests that, despite the minimal difference observed in some cases, the incorporation of CeNPs confers an enhanced antibacterial effect compared to the control.

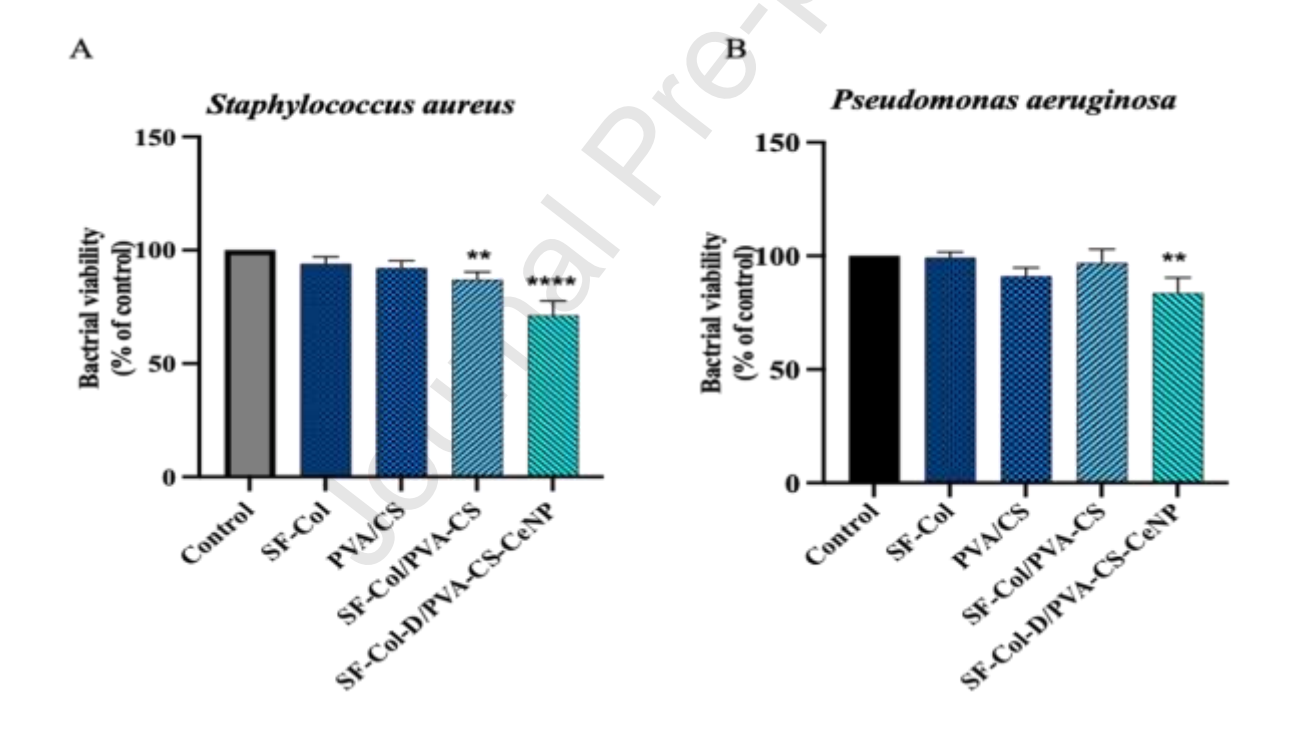


Fig 12. The survival results of (A) Gram-positive Staphylococcus aureus bacteria and (B) Gram-negative Pseudomonas aeruginosa bacteria with electrospun nanofibers. The data were shown in comparison with the control and as mean \pm SD, P****<0.0001 and P**<0.01.

3. 12. Macroscopic and microscopic wound analysis

A variety of animal models have been established to investigate type 2 diabetes (70-72); however, the patterns of disease development and progression in most of these models do not appear to correspond with the clinical presentation observed in humans. Numerous studies indicate that rats subjected to an HFD exhibit insulin resistance without the accompanying hyperglycemia (73, 74). Consequently, it has been proposed that HFD serves as a more effective approach for inducing insulin resistance, a pivotal characteristic of type 2 diabetes. Concurrently, streptozotocin (STZ) is commonly utilized to induce both insulin-dependent and non-insulindependent diabetes mellitus (75). While elevated doses of STZ considerably impair insulin secretion, resembling type 1 diabetes, lower doses of STZ lead to a mild impairment of insulin secretion that mirrors the attributes of type 2 diabetes in humans (70, 71). As a result, researchers have devised a rat model that combines an HFD with subsequent low-dose STZ administration, which has been proposed to effectively replicate the progression of type 2 diabetes from insulin resistance (76). In this study, administration of 30 mg/kg of STZ in conjunction with an HDF resulted in a significant elevation of blood glucose levels in fasting rats and manifested diabeticlike symptoms. This outcome is attributable to the diabetogenic properties of STZ, which induces necrosis and subsequently causes damage to pancreatic β-cell DNA (75). Such damage effectively impairs insulin synthesis in the affected rats, ultimately culminating in the development of a diabetic phenotype.

Moreover, the healing process of wounds in rats diverges markedly from that observed in humans, primarily due to differences in the contraction process. This distinction can be predominantly ascribed to the presence of a substantial subcutaneous striated muscle layer known as the panniculus carnosus, which is nearly absent in humans. In the case of rats, this muscle layer facilitates the independent movement of the skin relative to the deeper muscle

structures and is accountable for the accelerated contraction of the skin following wounding (77). In this paper, the discrepancy is effectively addressed in the developed diabetic wound model by encircling the wound with a silicone ring. Healing is facilitated through re-epithelialization, cellular proliferation, and angiogenesis, closely resembling the biological processes of wound healing in humans. Furthermore, the model is characterized by its simplicity, as intricate surgical techniques are not required. In this approach, a silicone ring is secured around the wound using an adhesive and is subsequently affixed to the surrounding skin sutures. (77).

The surgical procedure, encompassing wound creation, silicone ring suturing, scaffold grafting, and the ensuing wound healing process, is depicted in Fig. 13 A-D. Furthermore, images illustrating wounds from various groups at days 0, 3, 7, 14, and 21 post-wound creation are provided in Fig. 14A. This study involves an analysis and statistical comparison of the wound closure rate (Fig. 14B).

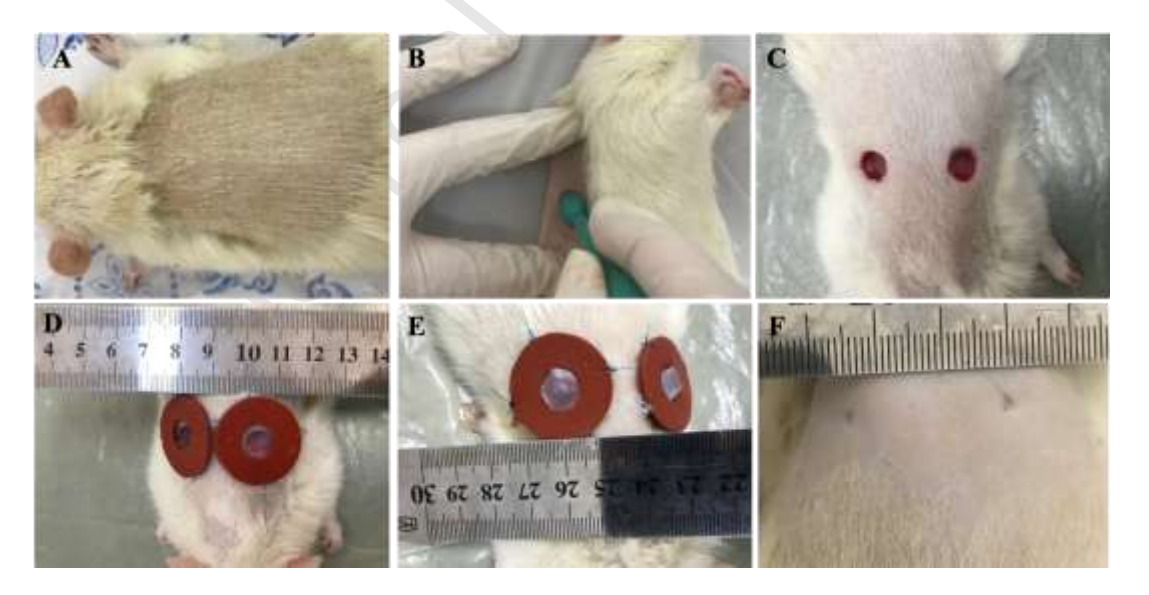


Fig. 13. (A-C) summary of the steps of creating the diabetic wound model; (D) silicone ring suture; (E) treatment with SF-Col-D/PVA-CS-CeNP nanofiber mat; and (F) wound healing after 21 days.



Fig. 14. (A) Macroscopic observation and wound closure rate in the studied rats. Images were taken on days 0, 3, 7, 14, and 21 post-surgery. (Scale 5 mm); (B) Percentage of wound area in the studied groups on days 0, 3, 7, 14, and 21. Data are expressed as mean \pm SD, n=3, $^{\#}$ P<0.05 and, * P<0.0001 compared to the diabetic control group.

As evidenced in the figures, on follow-up days, the treated group demonstrated a statistically significant reduction in the percentage of the wound area in comparison to the diabetic control group (Fig. 14B). In the histological study of wounds (Fig. 15A and B), blood cells are the predominant visible cellular across experimental groups three days post-surgery. The epithelium has completely regressed, and the formation of new epithelial tissue has yet to commence. By day 7, there is a notable reduction in blood cells, with inflammatory cells and fibroblasts comprising the majority of cells within the upper dermal layer. On the 14th day following wounding, immature granulation tissue becomes discernible in all groups, characterized by the presence of cells, developing small vessels, and newly synthesized collagen fibers oriented parallel to the wound surface. Furthermore, concurrent with the formation of the epidermis, the cellular count has significantly diminished, and collagen fibers have effectively enveloped the wound area. The collagen fibers initially identified as immature are progressively substituted with mature collagen by the conclusion of the healing period. Consequently, mature collagen fibers are evident in the histological images taken on day 21.

The wound-healing process in diabetic patients may result in chronic wound formation and the development of DFU (78). In diabetic wounds, a continuous inflammatory response is observed,

with the transition from the inflammatory phase to the proliferative phase being delayed due to the prolonged duration of the inflammatory phase and the activation of inflammatory cells (79). There is an increased release of inflammatory mediators, such as tumor necrosis factor (TNF) and interleukin-6 (IL-6), at the wound site, which effectively impedes the necessary cell proliferation and migration required for diabetic wound healing (80). The overactivation of inflammation leads to an elevated expression of matrix metalloproteinase (MMP-9) (81, 82), which results in the rapid degradation of normal collagen, fibronectin, and elastin, thereby further delaying the healing process of diabetic wounds (83). Indeed, diabetic vasculopathy, diminished angiogenesis, ischemia, and chronic inflammation contribute to a chronic inflammatory state for the wound, hindering its progression to subsequent stages of healing (84, 85).

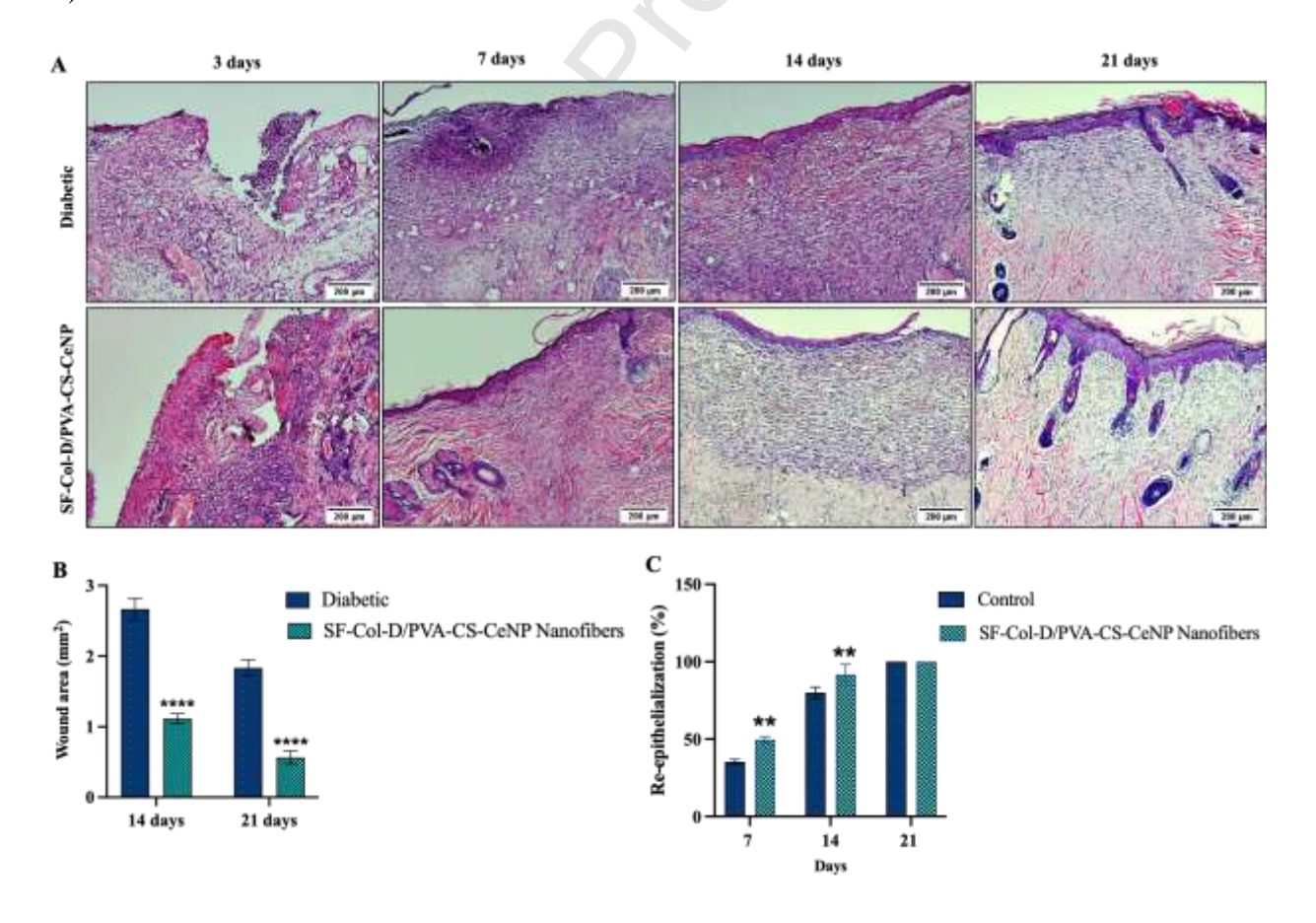


Fig. 15. (A) Images of H&E stained sections on days 3, 7, 14, and 21 in the studied groups (Scale 200 μ m); (B) Size of the wound area; (C) re-epithelialization in the wound area, results are shown as mean \pm SD, n=3, ****P<0.0001 and **P<0.05 compared to the diabetic control group.

Various studies have utilized silk, collagen, vitamin D, and other biomaterials as wound dressings. Studies have indicated that the strontium-loaded SF/SA blend films (particularly those prepared by treating with 5 mg/ml Sir solution) fulfill the requirements of a wound dressing, such as water absorption, water vapor transmission rate, mechanical properties, fibroblast cytocompatibility, angiogenesis, and antibacterial activity (85). Additionally, one study reported that collagen hydrolysate extracted from bovine tendons or rabbit skin, when mixed with chitosan and containing dill and/or lemon balm essential oils, exhibits good biocompatibility (86). Furthermore, cerium nanoparticle (CeNP)-loaded polyvinyl alcohol (PVA) nanogels demonstrated rapid healing in the Ce-nGel-Glu-treated wound with reduced damage.

Fig. 15C illustrates the percentage of re-epithelialization within the wound area on days 7, 14, and 21. As depicted, on day 7, the percentage of epidermis in the wound area of the treatment group exhibited a statistically significant increase in comparison to the control group. The collagenous and non-collagenous proteins and expression of various growth factors, including EGF, keratinocyte growth factor (KGF), growth factor-alpha (TGF-α), hepatocyte growth factor (HGF), bFGF, as well as KGF receptor (KGF-R), and HGF receptor (HGF-R), actions a remarkable role in wound healing (87). Fig. 15 illustrates the histological images of skin wounds that were treated for 21 days with SF-Col-D/PVA-CS-CeNP nanofibrous membranes. Notably, the skin wounds treated with these structures exhibited marked indications of wound healing maturation, characterized by the presence of thick collagen fiber bundles and follicular regeneration. In a majority of rats treated by SF-Col-D/PVA-CS-CeNP nanofibrous membranes, the regeneration of epidermal layers was nearly complete. The wound area was noted to be

densely filled with connective tissue encircled by a newly formed dermal layer. These findings further substantiate the effectiveness of electrospun SF-Col-D/PVA-CS-CeNP nanofibers in promoting wound healing.

4. Conclusion

SF-Col and PVA-CS nanofibers embedded with vitamin D3 and cerium oxide nanoparticles (CeNPs) were produced using the co-electrospinning method. Furthermore, the wound healing efficacy of the resultant nanofibrous membranes was assessed in vivo and through histological observations. Higher concentrations of SF-Col led to fibers with large diameters. In SF-Col nanofibers, increasing the concentration of vitamin D3 also increased fiber diameters, aligning with previous studies on polymer-dopant interactions. MTT assay indicated that SF-Col nanofibers containing up to 2% vitamin D3 were cytocompatible. Higher concentrations resulted in reduced cell viability. For PVA-CS nanofibers, the incorporation of CeNPs, surface-modified with fetal bovine serum (FBS) to reach uniform distribution, demonstrated no adverse effects on cell viability. FTIR test confirmed the characteristic peaks of SF, Col, PVA, and CS and indicated successful polymer integration and the formation of stable molecular interactions. Hydrophilicity studies, through water contact angle measurements, confirmed that both SF-Col and PVA-CS nanofibers were ideal for cell attachment because of their hydrophilic nature. Cross-linking enhanced the contact angle slightly, and vitamin D3 and CeNPs did not significantly alter hydrophilicity. Swelling and weight-loss studies demonstrated that SF-Col nanofibers had the highest swelling capacity, which can enhance wound healing by retaining nutrients and moisture. Vitamin D3 and CeNPs did not significantly change degradation rates. Drug release studies exhibited a sustained release of vitamin D3 for SF-Col nanofibers, with

Journal Pre-proof

maximum release in the first 24 h. CeNPs release from SF-Col-D/PVA-CS-CeNP nanofibers revealed an initial rapid release followed by a sustained release profile, proper for immediate ROS scavenging and prolonged antioxidant activity. The treatment with SF-Col-D/PVA-CS-CeNP structures led to nearly complete epidermal regeneration in most rats, with dense connective tissue formation and a newly developed dermal layer, highlighting their effectiveness in wound healing. The comprehensive analysis indicates that SF-Col and PVA-CS nanofibers, loaded with vitamin D3 and CeNPs, exhibit promising potential for wound healing applications by providing controlled degradation, excellent cytocompatibility, enhanced biological activity, and sustained drug release.

Conflict of Interest

The authors declare no conflict of interest regarding the publication of this work.

Acknowledgments

This study was kindly supported by the Mashhad University of Medical Sciences through research grant number 400453.

References

- 1. Mallik AS, Fichter MA, Rieder S, Bilic G, Stergioula S, Henke J, et al. Fetoscopic closure of punctured fetal membranes with acellular human amnion plugs in a rabbit model. Obstetrics & Gynecology. 2007;110(5):1121-9.
- 2. Saito H, Taguchi T, Kobayashi H, Kataoka K, Tanaka J, Murabayashi S, et al. Physicochemical properties of gelatin gels prepared using citric acid derivative. Materials Science and Engineering: C. 2004;24(6-8):781-5.
- 3. Saeedi P, Petersohn I, Salpea P, Malanda B, Karuranga S, Unwin N, et al. Global and regional diabetes prevalence estimates for 2019 and projections for 2030 and 2045: Results from the International Diabetes Federation Diabetes Atlas. Diabetes research and clinical practice. 2019;157:107843.

- 4. Xu J, Gao J, Li H, Zhu Z, Liu J, Gao C. The risk factors in diabetic foot ulcers and predictive value of prognosis of wound tissue vascular endothelium growth factor. Scientific Reports. 2024;14(1):14120.
- 5. Ranjbar-Mohammadi M, Shiralipour M. Production of Multilayer Nanofibers Through Polyvinyl Alcohol/Parrotia Persica Extract and Polycaprolactone Combination. Arabian Journal for Science and Engineering. 2024:1-9.
- 6. Ranjbar-Mohammadi M, Shakoori P, Arab-Bafrani Z. Design and characterization of keratin/PVA-PLA nanofibers containing hybrids of nanofibrillated chitosan/ZnO nanoparticles. International Journal of Biological Macromolecules. 2021;187:554-65.
- 7. Ibrahim MA, Nasr G, Ahmed R, Kelany NA. Physical characterization, biocompatibility, and antimicrobial activity of polyvinyl alcohol/sodium alginate blend doped with TiO2 nanoparticles for wound dressing applications. Scientific Reports. 2024;14(1):5391.
- 8. Blanquer A, Kostakova EK, Filova E, Lisnenko M, Broz A, Mullerova J, et al. A novel bifunctional multilayered nanofibrous membrane combining polycaprolactone and poly (vinyl alcohol) enriched with platelet lysate for skin wound healing. Nanoscale. 2024;16(4):1924-41.
- 9. Khan NU, Chengfeng X, Jiang M-Q, Khan ZU, Razzaq A, Ullah A, et al. Obstructed vein delivery of ceftriaxone via poly (vinyl-pyrrolidone)-iodine-chitosan nanofibers for the management of diabetic foot infections and burn wounds. International Journal of Biological Macromolecules. 2024;277:134166.
- 10. Mohammadzadehmoghadam S, Dong Y. Electrospinning of silk fibroin-based nanofibers and their applications in tissue engineering. Electrospun Polymers and Composites: Elsevier; 2021. p. 111-46.
- 11. Dos Santos FV, Siqueira RL, de Morais Ramos L, Yoshioka SA, Branciforti MC, Correa DS. Silk fibroin-derived electrospun materials for biomedical applications: A review. International Journal of Biological Macromolecules. 2024;254:127641.
- 12. Fang Y, Liu Z, Jin Y, Huang Y, Zhou S, Tian H, et al. Electrospun high hydrophilicity antimicrobial poly (lactic acid)/silk fibroin nanofiber membrane for wound dressings. International Journal of Biological Macromolecules. 2024;277:133905.
- 13. Amirrah IN, Lokanathan Y, Zulkiflee I, Wee MMR, Motta A, Fauzi MB. A comprehensive review on collagen type I development of biomaterials for tissue engineering: From biosynthesis to bioscaffold. Biomedicines. 2022;10(9):2307.
- 14. Rittié L. Type I collagen purification from rat tail tendons. Fibrosis: Methods and Protocols. 2017:287-308.
- 15. Ranjbar-Mohammadi M, Zamani M, Prabhakaran M, Bahrami SH, Ramakrishna S. Electrospinning of PLGA/gum tragacanth nanofibers containing tetracycline hydrochloride for periodontal regeneration. Materials Science and Engineering: C. 2016;58:521-31.
- 16. Ranjbar-Mohammadi M, Bahrami SH. Electrospun curcumin loaded poly (ϵ -caprolactone)/gum tragacanth nanofibers for biomedical application. International journal of biological macromolecules. 2016;84:448-56.
- 17. Kahraman HT. Fabrication of electrospun PA66 nanofibers loaded with biosynthesized silver nanoparticles: investigation of dye degradation and antibacterial activity. Environmental Science and Pollution Research. 2024:1-14.
- 18. Li S-F, Hu T-G, Wu H. Development of quercetin-loaded electrospun nanofibers through shellac coating on gelatin: Characterization, colon-targeted delivery, and anticancer activity. International Journal of Biological Macromolecules. 2024;277:134204.

- 19. Ullah A, Yang H, Takemae K, Wang F, Lee S, Kim IS. Sustainable bioactive food packaging based on electrospun zein-polycaprolactone nanofibers integrated with aster yomena extract loaded halloysite nanotubes. International Journal of Biological Macromolecules. 2024;267:131375.
- 20. Umar M, Sastry KS, Al Ali F, Al-Khulaifi M, Wang E, Chouchane AI. Vitamin D and the pathophysiology of inflammatory skin diseases. Skin pharmacology and physiology. 2018;31(2):74-86.
- 21. Qi M, Li W, Zheng X, Li X, Sun Y, Wang Y, et al. Cerium and its oxidant-based nanomaterials for antibacterial applications: a state-of-the-art review. Frontiers in Materials. 2020;7:213.
- 22. Loeffelbein DJ, Rohleder NH, Eddicks M, Baumann CM, Stoeckelhuber M, Wolff K-D, et al. Evaluation of human amniotic membrane as a wound dressing for split-thickness skin-graft donor sites. BioMed research international. 2014;2014(1):572183.
- 23. Rockwood DN, Preda RC, Yücel T, Wang X, Lovett ML, Kaplan DL. Materials fabrication from Bombyx mori silk fibroin. Nature protocols. 2011;6(10):1612-31.
- 24. Rajan N, Habermehl J, Coté M-F, Doillon CJ, Mantovani D. Preparation of ready-to-use, storable and reconstituted type I collagen from rat tail tendon for tissue engineering applications. Nature protocols. 2006;1(6):2753-8.
- 25. Wsoo MA, Abd Razak SI, Bohari SPM, Shahir S, Salihu R, Kadir MRA, et al. Vitamin D3-loaded electrospun cellulose acetate/polycaprolactone nanofibers: Characterization, in-vitro drug release and cytotoxicity studies. International journal of biological macromolecules. 2021;181:82-98.
- 26. Ghorbani M, Ghajari G, Kondori BJ. The Effects of Acidified Nitrite on Wound Healing in Streptozotocin-Induced Diabetic Mice. Advanced Biomedical Research. 2024;13(1):97.
- 27. Cheng K-Y, Lin Z-H, Cheng Y-P, Chiu H-Y, Yeh N-L, Wu T-K, et al. Wound healing in streptozotocin-induced diabetic rats using atmospheric-pressure argon plasma jet. Scientific reports. 2018;8(1):12214.
- 28. Keirouz A, Zakharova M, Kwon J, Robert C, Koutsos V, Callanan A, et al. High-throughput production of silk fibroin-based electrospun fibers as biomaterial for skin tissue engineering applications. Materials Science and Engineering: C. 2020;112:110939.
- 29. Sukigara S, Gandhi M, Ayutsede J, Micklus M, Ko F. Regeneration of Bombyx mori silk by electrospinning—part 1: processing parameters and geometric properties. Polymer. 2003;44(19):5721-7.
- 30. Amiraliyan N, Nouri M, Kish MH. Electrospinning of silk nanofibers. I. An investigation of nanofiber morphology and process optimization using response surface methodology. Fibers and Polymers. 2009;10:167-76.
- 31. Li Z, Hu W, Zhao Y, Ren L, Yuan X. Integrated antibacterial and antifouling surfaces via cross-linking chitosan-g-eugenol/zwitterionic copolymer on electrospun membranes. Colloids and Surfaces B: Biointerfaces. 2018;169:151-9.
- 32. Wei K, Kim B-S, Kim I-S. Fabrication and biocompatibility of electrospun silk biocomposites. Membranes. 2011;1(4):275-98.
- 33. Radisavljevic A, Stojanovic DB, Perisic S, Djokic V, Radojevic V, Rajilic-Stojanovic M, et al. Cefazolin-loaded polycaprolactone fibers produced via different electrospinning methods: Characterization, drug release and antibacterial effect. European Journal of Pharmaceutical Sciences. 2018;124:26-36.

- 34. Wiogo HT, Lim M, Bulmus V, Yun J, Amal R. Stabilization of magnetic iron oxide nanoparticles in biological media by fetal bovine serum (FBS). Langmuir. 2011;27(2):843-50.
- 35. Wang Q, Perez JM, Webster TJ. Inhibited growth of Pseudomonas aeruginosa by dextran-and polyacrylic acid-coated ceria nanoparticles. International journal of nanomedicine. 2013:3395-9.
- 36. Cuahtecontzi-Delint R, Mendez-Rojas MA, Bandala ER, Quiroz MA, Recillas S, Sanchez-Salas JL. Enhanced antibacterial activity of CeO2 nanoparticles by surfactants. International Journal of Chemical Reactor Engineering. 2013;11(2):781-5.
- 37. Wang R, Liu J, Fan R, Du Y, Fu Y, Liu X, et al. Effect of Bsa Surface Modification on Enzyme-Mimetic Activity of Ceo2 Nanozyme. Available at SSRN 4907913.
- 38. Ling S, Qi Z, Knight DP, Shao Z, Chen X. FTIR imaging, a useful method for studying the compatibility of silk fibroin-based polymer blends. Polymer Chemistry. 2013;4(21):5401-6.
- 39. Zhang H, Li L-l, Dai F-y, Zhang H-h, Ni B, Zhou W, et al. Preparation and characterization of silk fibroin as a biomaterial with potential for drug delivery. Journal of Translational Medicine. 2012;10:1-9.
- 40. Safiri S, Kolahi A-A, Smith E, Hill C, Bettampadi D, Mansournia MA, et al. Global, regional and national burden of osteoarthritis 1990-2017: a systematic analysis of the Global Burden of Disease Study 2017. Annals of the rheumatic diseases. 2020;79(6):819-28.
- 41. Roy T, Maity PP, Rameshbabu AP, Das B, John A, Dutta A, et al. Core-shell nanofibrous scaffold based on polycaprolactone-silk fibroin emulsion electrospinning for tissue engineering applications. Bioengineering. 2018;5(3):68.
- 42. Mohammadzadehmoghadam S, Dong Y. Fabrication and characterization of electrospun silk fibroin/gelatin scaffolds crosslinked with glutaraldehyde vapor. Frontiers in Materials. 2019;6:91.
- 43. Cheng Y, Far BF, Jahanbakhshi M, Bahrami S, Tamimi P, Sedaghat M, et al. Exploring the potential of a polyvinyl alcohol/chitosan-based nanofibrous matrix for erythromycin delivery: fabrication, in vitro and in vivo evaluation. RSC advances. 2023;13(27):18450-60.
- 44. Liao J, Qu Y, Chu B, Zhang X, Qian Z. Biodegradable CSMA/PECA/graphene porous hybrid scaffold for cartilage tissue engineering. Scientific reports. 2015;5(1):9879.
- 45. Henricsdotter C, Ellegaard K, Klokker L, Bartholdy C, Bandak E, Bartels E, et al. Changes in ultrasound assessed markers of inflammation following intra-articular steroid injection combined with exercise in knee osteoarthritis: exploratory outcome from a randomized trial. Osteoarthritis and Cartilage. 2016;24(5):814-21.
- 46. Lin X-L, Gao L-L, Li R-x, Cheng W, Zhang C-Q, Zhang X-z. Mechanical property and biocompatibility of silk fibroin–collagen type II composite membrane. Materials Science and Engineering: C. 2019;105:110018.
- 47. Olvera Bernal RA, Olekhnovich RO, Uspenskaya MV. Chitosan/PVA nanofibers as potential material for the development of soft actuators. Polymers. 2023;15(9):2037.
- 48. Vert M, Li S, Spenlehauer G, Guérin P. Bioresorbability and biocompatibility of aliphatic polyesters. Journal of materials science: Materials in medicine. 1992;3(6):432-46.
- 49. Kim U-J, Park J, Kim HJ, Wada M, Kaplan DL. Three-dimensional aqueous-derived biomaterial scaffolds from silk fibroin. Biomaterials. 2005;26(15):2775-85.
- 50. Sheng X, Fan L, He C, Zhang K, Mo X, Wang H. Vitamin E-loaded silk fibroin nanofibrous mats fabricated by green process for skin care application. International journal of biological macromolecules. 2013;56:49-56.

- 51. Li H, Wang M, Williams GR, Wu J, Sun X, Lv Y, et al. Electrospun gelatin nanofibers loaded with vitamins A and E as antibacterial wound dressing materials. RSC advances. 2016;6(55):50267-77.
- 52. Rather HA, Thakore R, Singh R, Jhala D, Singh S, Vasita R. Antioxidative study of Cerium Oxide nanoparticle functionalised PCL-Gelatin electrospun fibers for wound healing application. Bioactive materials. 2018;3(2):201-11.
- 53. McCord JM, Fridovich I. Superoxide dismutase: an enzymic function for erythrocuprein (hemocuprein). Journal of Biological chemistry. 1969;244(22):6049-55.
- 54. Costantini E, Aielli L, Gualdi G, Baronio M, Monari P, Amerio P, et al. Pulsed Radiofrequency Electromagnetic Fields as Modulators of Inflammation and Wound Healing in Primary Dermal Fibroblasts of Ulcers. Bioengineering. 2024;11(4):357.
- 55. Kurusu RS, Demarquette NR. Surface modification to control the water wettability of electrospun mats. International Materials Reviews. 2019;64(5):249-87.
- 56. Azari P, Hosseini S, Murphy BP, Martinez-Chapa SO. Electrospun biopolyesters: hydrophobic scaffolds with favorable biological response. J Public Health Int. 2018;1:5-9.
- 57. Yang M, Yu S, Zhao P, Shi G, Guo Y, Xie L, et al. Fabrication of biologically inspired electrospun collagen/silk fibroin/bioactive glass composited nanofibrous to accelerate the treatment efficiency of wound repair. International Wound Journal. 2023;20(3):687-98.
- 58. Dhandayuthapani B, Varghese SH, Aswathy RG, Yoshida Y, Maekawa T, Sakthikumar D. Evaluation of Antithrombogenicity and Hydrophilicity on Zein-SWCNT Electrospun Fibrous Nanocomposite Scaffolds. International journal of biomaterials. 2012;2012(1):345029.
- 59. Zhang H. Development and Blood Compatibility Assessment of Electrospun Polyvinyl Alcohol Blended with Metallocene Polyethylene and Plectranthus Amboinicus (PVA/mPE/PA) for Bone Tissue Engineering. 2018.
- 60. Huang N, Yang P, Leng Y, Chen J, Sun H, Wang J, et al. Hemocompatibility of titanium oxide films. Biomaterials. 2003;24(13):2177-87.
- 61. Milleret V, Hefti T, Hall H, Vogel V, Eberli D. Influence of the fiber diameter and surface roughness of electrospun vascular grafts on blood activation. Acta biomaterialia. 2012;8(12):4349-56.
- 62. Manikandan A, Mani MP, Jaganathan SK, Rajasekar R, Jagannath M. Formation of functional nanofibrous electrospun polyurethane and murivenna oil with improved haemocompatibility for wound healing. Polymer Testing. 2017;61:106-13.
- 63. Chang M, Nguyen TT. Strategy for treatment of infected diabetic foot ulcers. Accounts of chemical research. 2021;54(5):1080-93.
- 64. Lu H-T, Huang G-Y, Chang W-J, Lu T-W, Huang T-W, Ho M-H, et al. Modification of chitosan nanofibers with CuS and fucoidan for antibacterial and bone tissue engineering applications. Carbohydrate Polymers. 2022;281:119035.
- 65. Gao Y, Bach Truong Y, Zhu Y, Louis Kyratzis I. Electrospun antibacterial nanofibers: Production, activity, and in vivo applications. Journal of Applied Polymer Science. 2014;131(18).
- 66. Salehi M, Naseri-Nosar M, Azami M, Nodooshan SJ, Arish J. Comparative study of poly (L-lactic acid) scaffolds coated with chitosan nanoparticles prepared via ultrasonication and ionic gelation techniques. Tissue engineering and regenerative medicine. 2016;13:498-506.
- 67. Santiago-Morales J, Amariei G, Letón P, Rosal R. Antimicrobial activity of poly (vinyl alcohol)-poly (acrylic acid) electrospun nanofibers. Colloids and Surfaces B: Biointerfaces. 2016:146:144-51.

- 68. Ramasamy M, Lee J. Recent nanotechnology approaches for prevention and treatment of biofilm-associated infections on medical devices. BioMed Research International. 2016;2016(1):1851242.
- 69. Farias IAP, Santos CCLd, Sampaio FC. Antimicrobial activity of cerium oxide nanoparticles on opportunistic microorganisms: a systematic review. BioMed research international. 2018;2018(1):1923606.
- 70. Reed M, Meszaros K, Entes L, Claypool M, Pinkett J, Gadbois T, et al. A new rat model of type 2 diabetes: the fat-fed, streptozotocin-treated rat. Metabolism-Clinical and Experimental. 2000;49(11):1390-4.
- 71. Srinivasan K, Viswanad B, Asrat L, Kaul C, Ramarao P. Combination of high-fat diet-fed and low-dose streptozotocin-treated rat: a model for type 2 diabetes and pharmacological screening. Pharmacological research. 2005;52(4):313-20.
- 72. Franconi F, Seghieri G, Canu S, Straface E, Campesi I, Malorni W. Are the available experimental models of type 2 diabetes appropriate for a gender perspective? Pharmacological research. 2008;57(1):6-18.
- 73. Zhao S, Chu Y, Zhang C, Lin Y, Xu K, Yang P, et al. Diet-induced central obesity and insulin resistance in rabbits. Journal of animal physiology and animal nutrition. 2008;92(1):105-11.
- 74. Flanagan AM, Brown JL, Santiago CA, Aad PY, Spicer LJ, Spicer MT. High-fat diets promote insulin resistance through cytokine gene expression in growing female rats. The Journal of nutritional biochemistry. 2008;19(8):505-13.
- 75. Szkudelski T. The mechanism of alloxan and streptozotocin action in B cells of the rat pancreas. Physiological research. 2001;50(6):537-46.
- 76. Zhang M, Lv X-Y, Li J, Xu Z-G, Chen L. The characterization of high-fat diet and multiple low-dose streptozotocin induced type 2 diabetes rat model. Journal of Diabetes Research. 2008;2008(1):704045.
- 77. Dunn L, Prosser HC, Tan JT, Vanags LZ, Ng MK, Bursill CA. Murine model of wound healing. Journal of visualized experiments: JoVE. 2013(75):50265.
- 78. Boulton AJ, Vileikyte L, Ragnarson-Tennvall G, Apelqvist J. The global burden of diabetic foot disease. The Lancet. 2005;366(9498):1719-24.
- 79. Wang W, Yan X, Lin Y, Ge H, Tan Q. Wnt7a promotes wound healing by regulation of angiogenesis and inflammation: Issues on diabetes and obesity. Journal of Dermatological Science. 2018;91(2):124-33.
- 80. Wang Y, Liu J, Kong Q, Cheng H, Tu F, Yu P, et al. Cardiomyocyte-specific deficiency of HSPB1 worsens cardiac dysfunction by activating NFκB-mediated leucocyte recruitment after myocardial infarction. Cardiovascular research. 2019;115(1):154-67.
- 81. Nguyen TT, Ding D, Wolter WR, Champion MM, Hesek D, Lee M, et al. Expression of active matrix metalloproteinase-9 as a likely contributor to the clinical failure of aclerastide in treatment of diabetic foot ulcers. European journal of pharmacology. 2018;834:77-83.
- 82. Wang W, Yang C, Wang XY, Zhou LY, Lao GJ, Liu D, et al. MicroRNA-129 and-335 promote diabetic wound healing by inhibiting Sp1-mediated MMP-9 expression. Diabetes. 2018;67(8):1627-38.
- 83. Zhuge Y, Regueiro MM, Tian R, Li Y, Xia X, Vazquez-Padron R, et al. The effect of estrogen on diabetic wound healing is mediated through increasing the function of various bone marrow-derived progenitor cells. Journal of vascular surgery. 2018;68(6):127S-35S.

- 84. Spampinato SF, Caruso GI, De Pasquale R, Sortino MA, Merlo S. The treatment of impaired wound healing in diabetes: looking among old drugs. Pharmaceuticals. 2020;13(4):60.
- 85. Yang P, Pei Q, Yu T, Chang Q, Wang D, Gao M, et al. Compromised wound healing in ischemic type 2 diabetic rats. PloS one. 2016;11(3):e0152068.
- 86. Râpă M, Gaidau C, Mititelu-Tartau L, Berechet M-D, Berbecaru AC, Rosca I, et al. Bioactive collagen hydrolysate-chitosan/essential oil electrospun nanofibers designed for medical wound dressings. Pharmaceutics. 2021;13(11):1939.
- 87. Koizumi N, Inatomi T, Sotozono C, Fullwood NJ, Quantock AJ, Kinoshita S. Growth factor mRNA and protein in preserved human amniotic membrane. Current eye research. 2000;20(3):173-7.

Journal Pre-proof

Declaration of interests

with authors declare that they have no known competing imancial interests of personal relationship	15
that could have appeared to influence the work reported in this paper.	
☐ The authors declare the following financial interests/personal relationships which may be considered	ed
as potential competing interests:	